Final Report

Bingham Mine Cold-Air Pool Structure and Evolution

C. David Whiteman, Ph.D.
Research Professor

Sebastian W. Hoch, Ph.D
Research Assistant Professor

30 November 2014

Department of Atmospheric Sciences
University of Utah
135 S 1460 E, Rm 819
Salt Lake City, UT 84112-0110

1. Introduction

In the winter of 2010-2011 a major federally funded field research program called the Persistent Cold-Air Pool Study (PCAPS) was initiated to investigate the meteorological influences on wintertime temperature inversions that were leading to air quality problems in Utah's Salt Lake Valley. In connection with this federally funded research program the University of Utah (UU) and Kennecott Utah Copper (KUC) initiated a 3-year Research Agreement to extend the meteorological investigations to the Bingham Canyon Mine (BCM). This research program was called the Bingham Mine Cold-Air Pool Structure and Evolution Experiment or the Bingham Canyon Mine Experiment. This research program was later extended by 1 year to encompass 4 winters. As part of this program, wintertime meteorological data collected by UU inside and outside the mine were used to supplement meteorological data collected routinely by KUC. These data have been analyzed and reported in monthly reports, conference proceedings, peer-reviewed journal papers and a master's thesis, and are publicly available. Presentations have also been made to KUC and the Utah Department of Air Quality (UDAQ). During the course of the research, Approval Order DAQE-AN0105710028-11 was issued on 27 June 2011 by UDAQ to allow an increase in the amount of ore and waste rock moved in a 12-month period to 260,000,000 tons in the Bingham Canyon Mine. As a condition of the Approval Order, KUC was to design a protocol to further evaluate the pit escape fractions at the BCM using modeling and a field study, as the pit escape fractions (20% for PM_{10} and 21% for $PM_{2.5}$) that had been used for modeling the transport of emissions from the mine were deemed to need further study. These pit escape fractions had been determined in a Computational Fluid Dynamics modeling study conducted as part of a University of Utah master's thesis by Bhaskar and Tandon (1996). It is well known that aerosol release fractions will vary from day to day depending on meteorology. It was convenient and approved, however, to use conservative single fixed values for air quality modeling. Additional computations of worst-case release fractions of 22 and 33% were presented in Appendix A to the Bhaskar and Tandon (1996) study, depending on whether particles hitting the ground were deposited or reflected back into the atmosphere. It is generally thought that the smallest release fractions will occur in quiescent cold-air pool (high atmospheric stability) conditions in winter and that the largest release fractions will occur in any season when strong winds are present within the mine and the atmosphere is unstable.

While the Bingham Canyon Mine Experiment was originally envisioned as an investigation of the meteorology of the mine during wintertime cold-air pool conditions, we have also applied the improved meteorological knowledge to gain a better understanding of the pit escape issue. Thus, this final report, while focused on the meteorology of the mine, also suggests an observational and mathematical approach to evaluate the pit escape fraction. We illustrate this approach by applying it to a typical winter inversion period using data from January 2014. The results are merely illustrative of the method and, because a major assumption had to be made regarding the aerosol characteristics inside the mine in the absence of actual data, the results are not considered to be definitive. They are illustrative of the approach, however, and we propose the new method as an alternative or supplement to other methods.

This report focuses on the wintertime meteorology at the BCM during an extended cold-air pool or "inversion" episode that occurred from 14 to 28 January 2014. The report begins by

describing the mine topography and meteorological measurements, followed by a description of the general weather situation that led to the multi-day episode and the exceedances of the PM$_{2.5}$ National Ambient Air Quality Standards (NAAQS) that were observed in the adjacent Salt Lake City urban area below the mine. Meteorological measurements inside the mine and in its surroundings are analyzed to determine the meteorological mechanisms that produce diurnal changes in the mine atmosphere leading to air mass removal from the mine. An aerosol lidar (ceilometer) placed inside the mine provided crucial data supporting the meteorological conclusions. The availability of the lidar data also suggested to us a new method for computing release fractions. The report thus continues with a description of the method and its mathematical basis. The method's accuracy will depend on the development of a backscatter-aerosol concentration relationship for the actual aerosols inside the mine. Unfortunately, data to develop this relationship are not yet available. Thus, to illustrate the method we use a backscatter-aerosol concentration relationship developed for the adjacent Salt Lake Valley. Because of the uncertainty involved in using the Salt Lake City backscatter-concentration relationship, the results should not be used for decision-making, but rather for illustration of the method. Using emission estimates from the mine, estimates are made of the particle *ventilation fraction* (the fraction of particles suspended in the mine atmosphere that leave the mine), the dry deposition of particulates within the mine and the particulate *escape fraction* (the fraction of particulate emissions that leave the mine). The advantages and disadvantages of the new methodology are then discussed, and conclusions are drawn from the study. The report ends with suggestions of future analyses that could strengthen the scientific basis of the meteorological and air quality findings. We hope that this new methodology will prove useful in gaining an understanding of the wintertime ventilation of the Bingham Mine and that the technique will prove useful in other meteorological situations and in other settings.

2. Topography, meteorological measurements, air quality, and weather summary

2.1 Topography and meteorological sites

The Bingham Canyon Mine (BCM) is a large open-pit mine that is thought to be the deepest manmade excavation on Earth (Pankow et al. 2013). It is located on the east slope of the Oquirrh Mountains at the southwest end of the Salt Lake Valley (SLV). The topography of the SLV, the location of the BCM and selected meteorological and air quality measurement sites are shown in Figure 1. Higher resolution topography of the BCM and the locations of selected meteorological measurement sites in the vicinity of the BCM are shown in Figure 2. Excavation is continuing in the mine so that the topography is ever changing. The topography in this figure comes from a digital elevation model produced before the 10 April 2013 landslide. The ridgeline that confines the mine airshed is indicated on this figure, and elevations on this ridgeline are shown in Figure 3. The mine volume and drainage area as functions of altitude are presented in Figure 4. The lowest opening into the mine (1973 m MSL) is at the mine's north side at Bingham Pass. The BCM is largely unconfined on its east side for altitudes above about 2200 m MSL. Much of the waste rock removed from the mine is transported via haul trucks through Bingham Pass to waste dumps north of the mine.
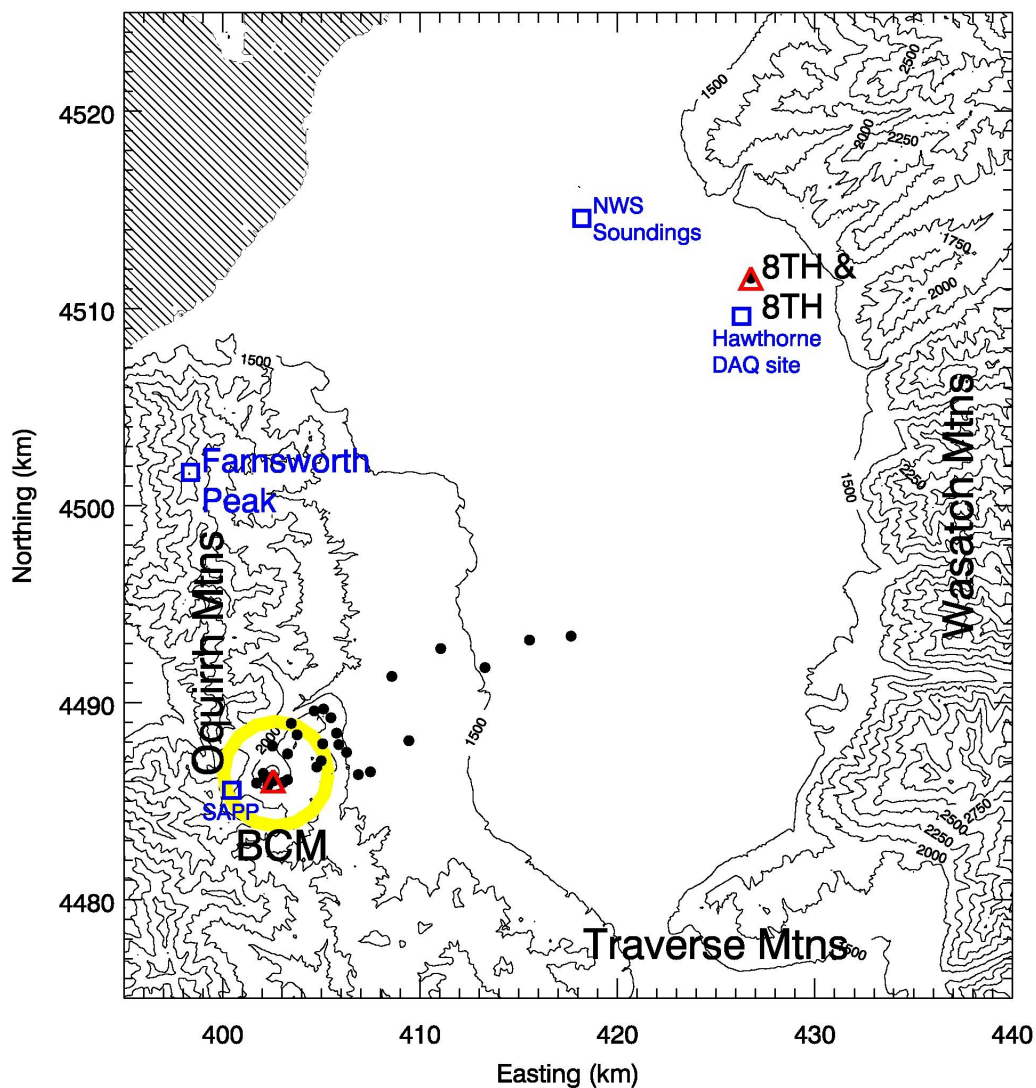
Figure 1. Topographic map (UTM coordinates, zone 12, 250-m elevation contours) of the Salt Lake Valley, showing the measurement sites during winter 2013-2014. Red triangles denote ceilometer locations in the BCM and near 8th East and 8th South, black dots denote automatic temperature and humidity sensors; blue squares show sites providing additional meteorological data including the SAPP KUC automatic weather station, the DAQ air quality station at Hawthorne Elementary School where $PM_{2.5}$ and PM_{10} measurements were made, the Salt Lake City airport where radiosondes were launched, and Farnsworth Peak where weather station data were available from MesoWest.
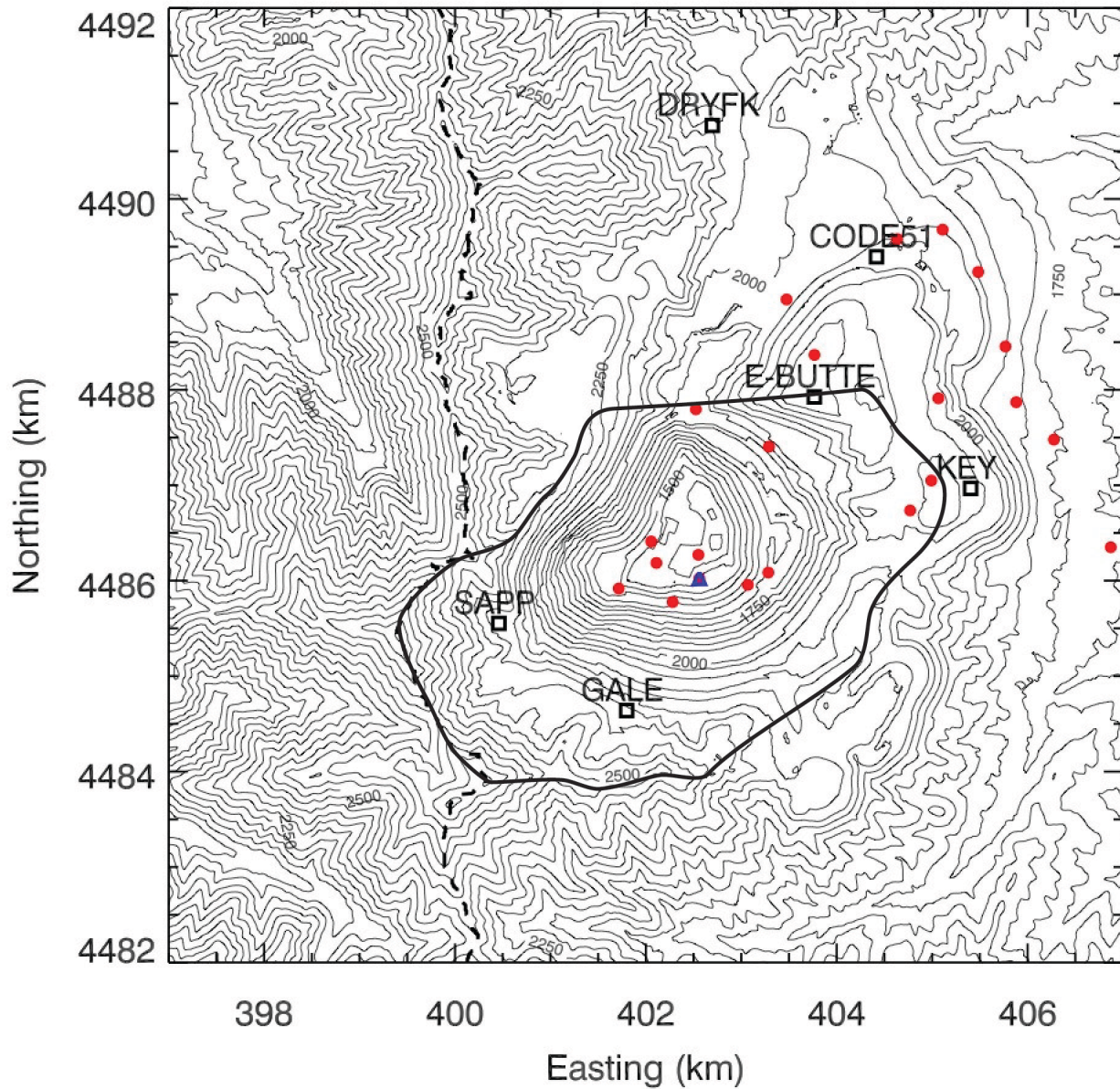
Figure 2. Topographic map (UTM coordinates, zone 12, 50-m contours) showing meteorological measurement sites in and around the BCM during winter 2013-2014. The open squares are KUC automatic weather stations, the red dots are HOBO® automatic temperature data loggers, and the blue triangle is the ceilometer. An additional 7 automatic temperature data loggers (see Figure 1) ran ENE toward West Jordan. The airshed boundaries of the mine used in calculating drainage area and volume is indicated by the thick black contour.
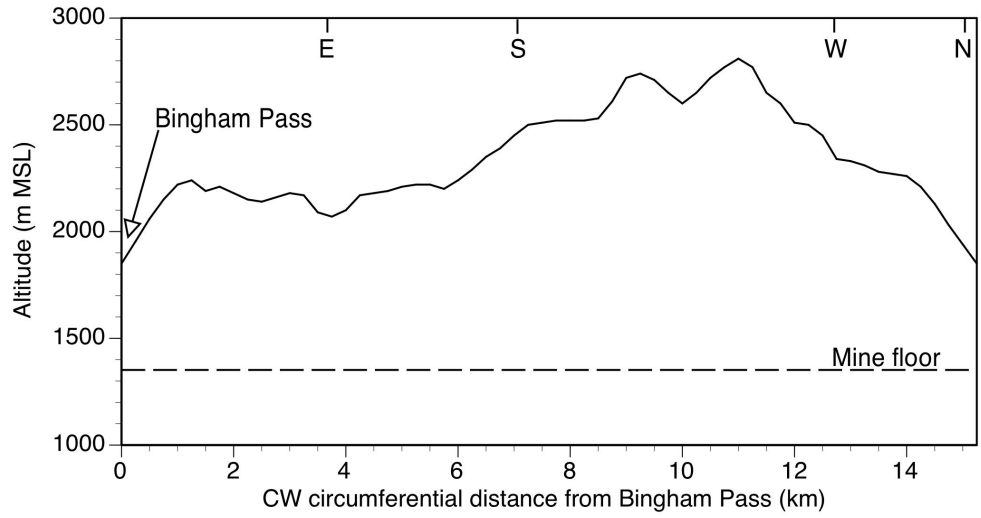
Figure 3. Altitudes on the circumference of the BCM as measured clockwise from near Bingham Pass along the ridgeline indicated in Figure 2.
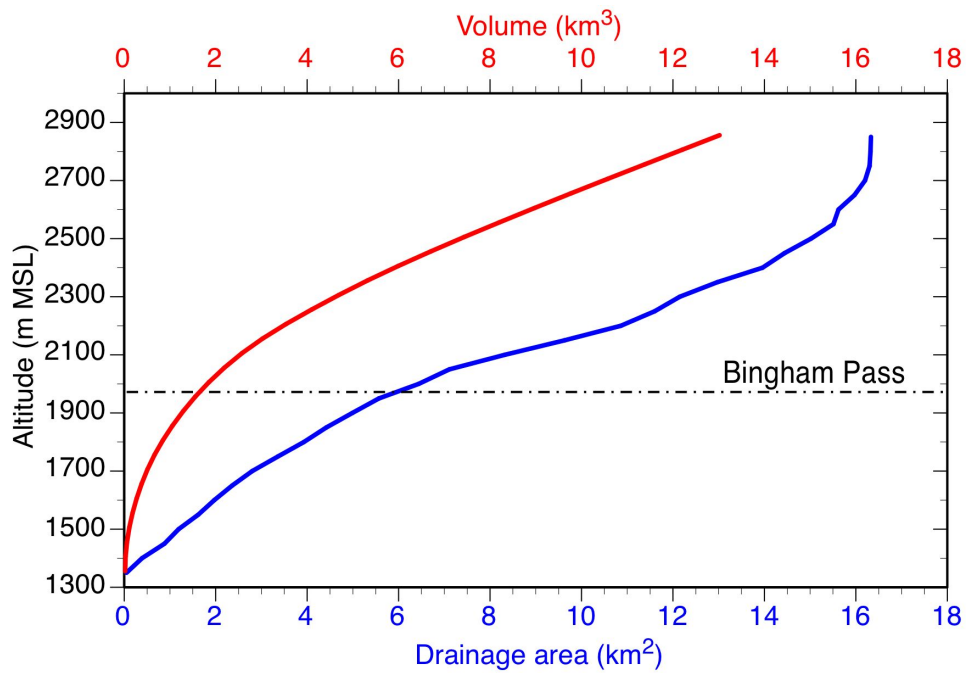

Figure 4. BCM drainage area and volume as a function of altitude.

2.2 Air quality in the SLV during the 15-day period 14-28 January 2014

The choice of the 14-28 January period for our analyses was determined based on the unusually good meteorological data sets available (especially from the ceilometer in the mine), and the fact that fine aerosol particle exceedances occurred frequently in the nearby SLV during this period of typical mid-winter non-cloudy cold-air pools.

Criteria pollutants emitted in the SLV and BCM include particles with aerodynamic diameter ≤ 2.5 μm ($PM_{2.5}$) and ≤ 10 μm (PM_{10}). Gravitational settling velocities for particles of different sizes are listed in Table 1. Large particles (e.g. 100 μm) settle very quickly. In a 17-h stagnation period, 1 μm particles would fall only 6 cm relative to still air, 2.5 μm particles would fall about 12 m , and 10 μm particles would fall over 300 m.

Table 1. Terminal gravitational settling velocities and settling times for particles of different aerodynamic diameter. From Lapple (1961)

Aerodynamic diameter (μm)	100	10	2.5	1
Settling velocity (cm s^{-1})	50	0.5	0.02	0.0001
Time to settle 1 meter	2 sec	3.3 min	83 min	11.5 days
Settling distance in 17 hours	30,600 m	306 m	12	0.06 m

The *daily* 24-h-average values of $PM_{2.5}$ and PM_{10} from midnight to midnight MST at the Hawthorne Elementary School in the Salt Lake Valley are shown for the 15-day period in Figure 5. The 24-h-average NAAQS for PM_{10} (150 μg m^{-3}) was not exceeded during this period. The 24-h-average NAAQS for $PM_{2.5}$ (35 μg m^{-3}) was exceeded, however, on 18, 19, 20, 21, 22, 23, 26 and 27 January 2014. During this period, $PM_{2.5}$ made up 64% of the PM_{10} mass concentrations.

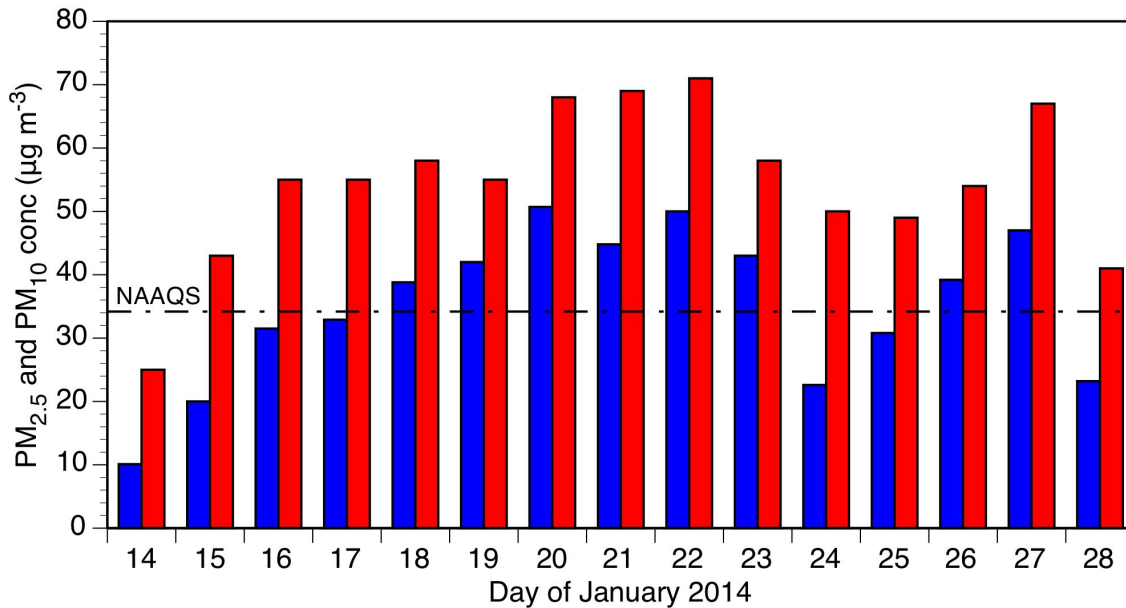Figure 5. Daily mean $PM_{2.5}$ (blue) and PM_{10} (red) concentrations at Hawthorne Elementary School in the SLV during the 14-28 January 2014 period, as reported by UDAQ from Federal Reference Method filter samplers. The dot-dash line is the 35 μg m^{-3} 24-h-mean NAAQS for $PM_{2.5}$. The 24-h-mean NAAQS for PM_{10} is 150 μg m^{-3}.

Hourly $PM_{2.5}$ and PM_{10} concentrations were also measured at Hawthorne Elementary School by UDAQ during the 15-day period (**Figure 6**). There is a marked diurnal variation in concentrations for both particulate sizes, with concentrations lowest near sunrise and highest between noon and late evening. $PM_{2.5}$ and PM_{10} concentrations are not measured at the BCM.
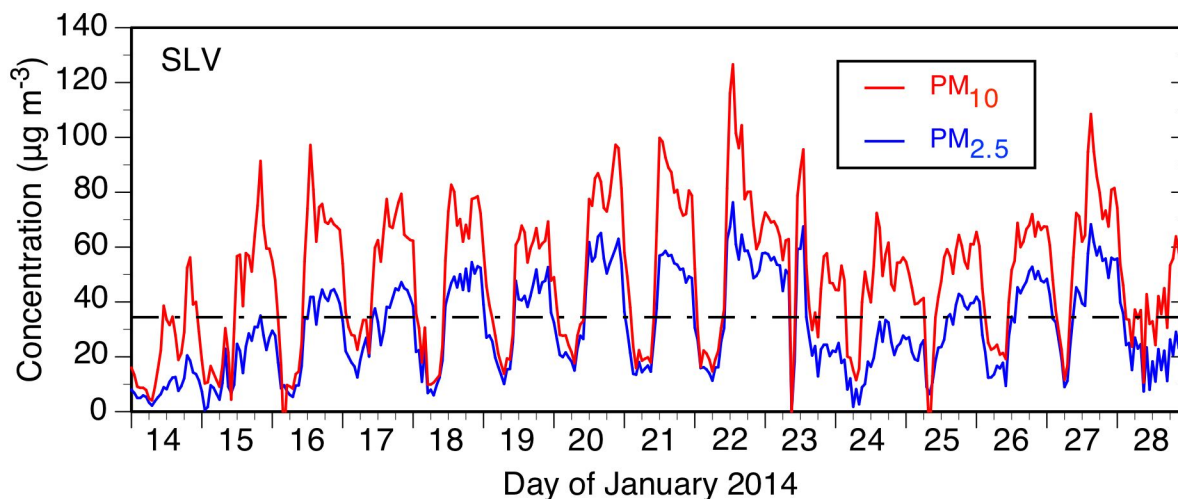

Figure 6. Hourly $PM_{2.5}$ and PM_{10} concentrations at Hawthorne Elementary School during the 15-day period. The 24-hour-average NAAQS for $PM_{2.5}$ is indicated by the horizontal line.

2.3. General weather conditions during the 15-day period

A semi-permanent, high-pressure ridge was nearly stationary over Utah during the 15-day period. A 500-mb upper-air weather chart for 17 January is shown as an example in Figure 7. The chart shows the typical light northwesterly winds aloft that occur over the SLV during cold-air pools. Weather charts for all days of the 15-day episode are provided in Appendix A. Radiosondes launched twice per day from the Salt Lake City airport at 0500 and 1700 MST provide vertical profiles of temperature, humidity, wind direction and wind speed. Soundings for 17 January 2014 (Figure 8) are typical. Temperatures are in a narrow diurnal range near freezing with a surface-based temperature inversion extending to heights of 1600 to 1900 m MSL and with subsidence inversions above mountain top level. The subsidence associated with high-pressure ridges produces clear skies with low to moderate humidity aloft but higher humidity near the valley floor, especially at night. The light northwesterly winds aloft turn into a down-valley direction or become light and variable within the valley. Additional soundings during the 15-day period are provided in Appendix B.
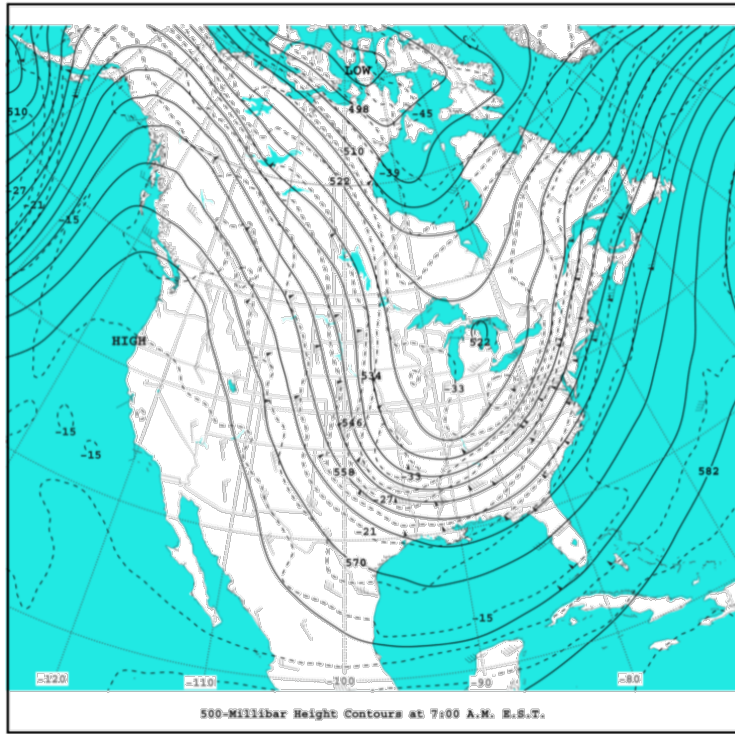
Figure 7. 500 mb weather chart for 17 January 2014, illustrating the high-pressure ridge that was stationary over the western U.S. during the experimental period.
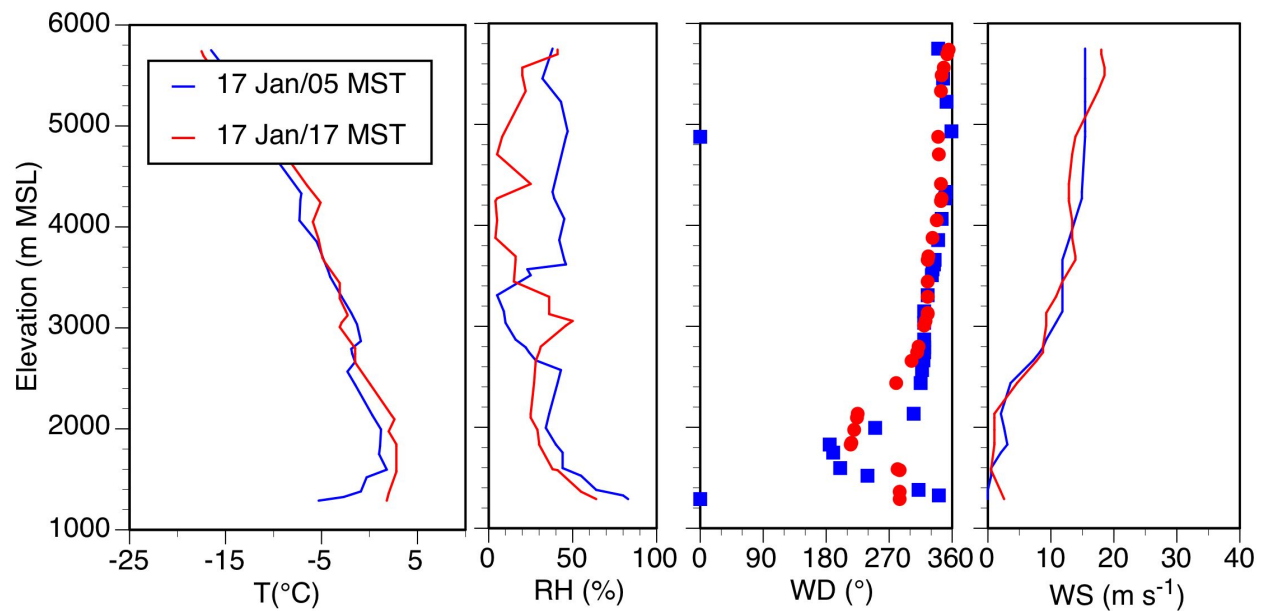

Figure 8. 17 January 2014 0500 MST and 17 January 2014 1700 MST radiosonde soundings of temperature, humidity, wind direction and wind speed in the Salt Lake Valley, illustrating soundings typical of wintertime cold-air pools. Data from the National Weather Service.

9

2.4. Aerosol backscatter during the 15-day period

Two University of Utah Vaisala Model CL31 ceilometers (Figure 9) were operated during the winter of 2013-2014. One was deployed in the BCM at an elevation 84 m above the mine floor at 1457 m MSL and the other near 8th East and 8th South in Salt Lake City at 1309 m MSL. The CL31 ceilometer is a vertically pointing 910 μm (i.e., near-infrared wavelength) laser that emits 10,000 light pulses per second. Backscatter coefficient profiles are recorded every 16 seconds from the light scattered back by aerosols. Time-height cross-sections of aerosol backscatter profiles are produced as the main product of the ceilometer measurements. Young (2012) and Young and Whiteman (2014) used time-height cross-sections from the same model ceilometer to gain understanding of the meteorology and air quality for cold-air pool events that occurred in the SLV in the winter of 2010-2011. Software and communication protocols were developed to display these plots on a University of Utah website in near-real time during the 2013-2014 inversion season (http://home.chpc.utah.edu/~u0453210/PM2.5/PM2.5.html). The CL31 differs from previous ceilometers in having the same optical path for both the transmitted and backscattered light, as the emitted beam is sent through a small hole in the mirror of the receiving telescope. This single optical path greatly improves the performance of the ceilometer at distances close to the transmitter.

Figure 9. CL31 Ceilometer deployed in the Bingham Canyon Mine, with a temperature/humidity data logger in the background.

Time-height cross-sections of the backscatter coefficient from the two ceilometers are shown in Figure 10 for the SLV and BCM sites for the 15-day cold-air pool episode. The top of the

aerosol layer is shown as a black line, as determined using a backscatter threshold method with a threshold of $10^{-6.75}$ sr^{-1} m^{-1} (Melfi et al. 1985; Emeis 2011). The logarithmic scaling of the backscatter coefficient emphasizes weaker backscatter values. The green triangular areas projecting down from the tops of the figures on a daily basis are sunlight that is scattered into the optical axis of the receiving telescope to produce a weak signal, an artifact that should be ignored. Aerosols from the SLV do not usually extend to the elevation of Bingham Pass. Aerosols at BCM, however, extend above Bingham Pass and East Ridge every day. Backscatter coefficients are higher in the BCM than in the SLV and the backscatter coefficients in the mine are more evenly distributed in the vertical than for the SLV, probably because aerosols produced by the haul trucks within the mine are emitted over a range of altitudes. The diurnal aerosol pattern within the mine is quite regular in comparison to the diurnal pattern in the SLV. This is because the SLV is more open to meteorological influences, aerosol pollutant sources are more diverse and mostly located on the valley floor, and the sources are more variable in time.
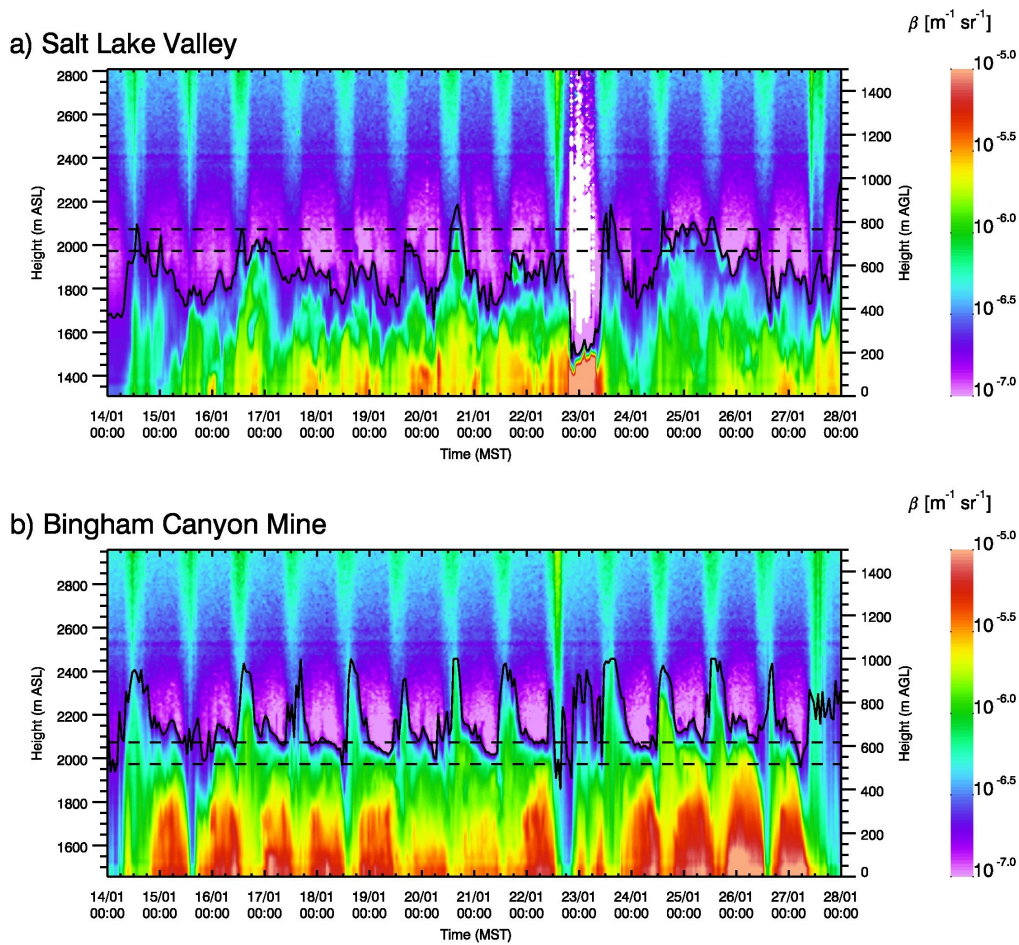

Figure 10. Ceilometer backscatter coefficient (m^{-1} sr^{-1}) plotted on a log$_{10}$ scale for a) the SLV and b) the BCM. The black solid line indicates the top of the aerosol layer. The horizontal dashed lines indicate the elevations of Bingham Pass (1973 m MSL) and the lowest point on the mine's East Ridge (2073 m MSL).

While Figure 10 is a portrayal of the entire episode on a single plot, we have also produced daily plots for the episode. An example for the representative day of 17 January 2014 is shown in Figure 11, where aerosol concentrations are well diffused vertically in the late afternoon, but accumulate at elevations near the crusher level (~1680 m MSL) beginning at about 2200 MST. Heavier accumulations then build up in the lowest 150 m of the ceilometer range from midnight to about 0730 MST. Following sunrise the aerosols in the lowest elevations of the mine begin to be diffused vertically. A daily ventilation process begins when relatively clean air descends into the mine starting at around 0900-1000 MST. Much of the aerosol burden is mixed out of the mine by mid-afternoon.
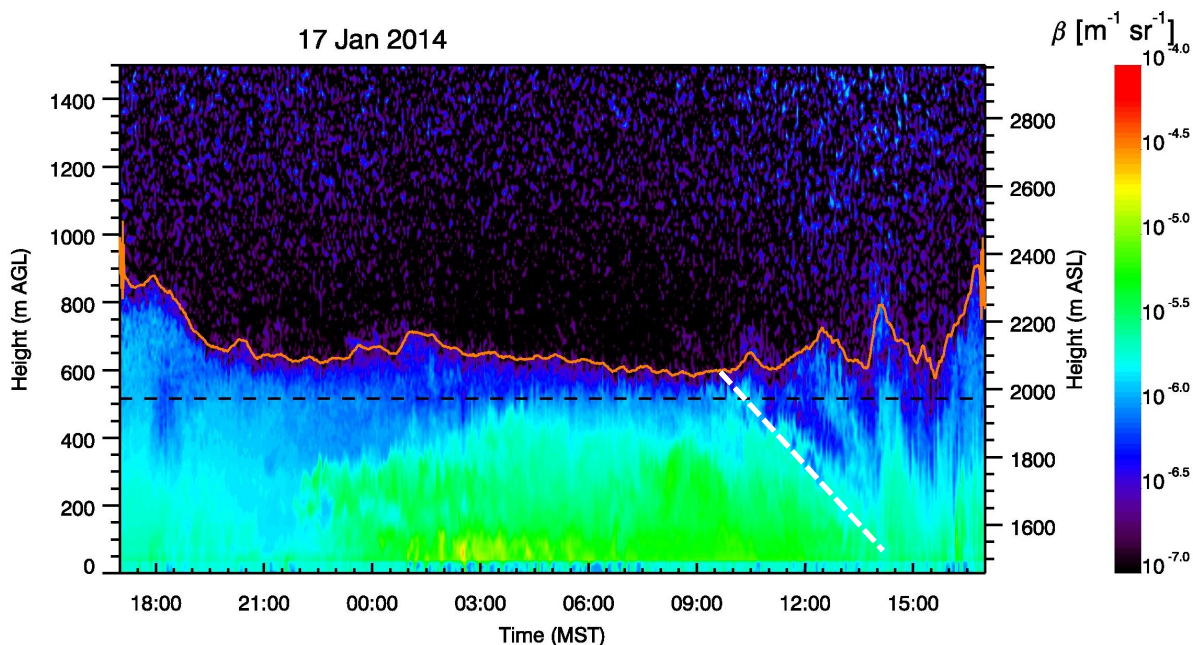

Figure 11. Backscatter coefficient as a function of height and time for 17 January 2014. The orange line is the top of the aerosol layer. The black dashed line is the elevation of Bingham Pass, and the dashed white line indicates the sinking of cleaner air into the mine.

The ceilometer backscatter coefficient is related to atmospheric aerosol concentration. The relationship, however, is known from theory to be dependent on aerosol size, composition and humidity (Sundström et al. 2009). No information on aerosol size or composition is available from BCM. Of particular importance is the size distribution of aerosols. Small diameter aerosols such as $PM_{2.5}$ can be produced through in-atmosphere chemical reactions of precursor gases including NOx, SO_2 and volatile organic compounds (VOCs). These precursor gases are present inside the mine, with estimated emission rates reported to regulatory agencies. There is no information on precursor concentrations, chemical mechanisms, reaction rates, and resulting particle characteristics, whose states are dependent on temperature and humidity.

3. Meteorology leading to particulate release during cold-air pools

3.1 Aerosol release mechanism

We begin with a conceptual description of the aerosol release mechanism, to be followed by analyses of data confirming the concepts. We have already shown that aerosol escape from the BCM occurs on a daily basis during non-cloudy wintertime cold-air pool episodes (Figure 10b). The escape occurs during daytime beginning at about 0900 and ending at about 1700 MST on typical days. The winter insolation (i.e., solar radiation intensity) on the south-facing wall of the BCM is the main cause of the daytime aerosol escape. The rock walls absorb the solar radiation, convection begins over the heated slope, and an upslope flow is initiated over this sidewall. The upslope layer progresses deeper into the mine during the morning as the sun rises to its zenith and retreats up the south-facing sidewall in the afternoon as the sun descends. Compensatory sinking motions occur over the basin center bringing cleaner air into the basin to compensate for the polluted air being carried up the slope. This compensatory sinking, which begins around 0900 MST, is supplemented by weak downslope flows that occur over the southern, snow-covered sidewall, which persist during the night and most of the day. A cross-basin flow that develops from the cold sidewall to the heated sidewall carries aerosols toward the upslope flow layer where they are entrained or fumigated into the layer and carried up the slope. The material carried up the slope is vented into the upper part of the basin and into the air above the mine basin where it is carried away from the pit by ambient flows at that altitude.

These meteorological mechanisms leading to aerosol escape have been previously documented for other valleys and basins. Here we present a short summary of selected literature. A simple numerical model of pollutant mass entrainment into growing upslope flows during the post-sunrise temperature inversion breakup period was published in 1978 (Whiteman and McKee 1978). The post-sunrise inversion destruction mechanism was described (Whiteman 1982) and an analytical model was developed that successfully simulated inversion destruction in Colorado valleys (Whiteman and McKee 1982). Bader and McKee (1983, 1985) and Bader and Whiteman (1989) used a full-physics numerical model to demonstrate the mechanism. Two air quality models were developed for the Environmental Protection Agency to simulate the effects of the mechanism on air quality in valleys (Whiteman and Allwine 1985; Allwine et al. 1997) and its effect on the transport of pollutants from valleys into regional scale flows (Allwine and Whiteman 1983, 1984, 1985, 1988). A sulfur hexafluoride tracer experiment in Colorado's Brush Creek Valley confirmed that tracer material was transported across a north-south valley towards the east-facing sidewall that was heated by the morning sun (Whiteman 1989) and its subsequent fumigation of the slope and transport up the valley sidewall and dispersion into regional flows. Cross-basin flows that occur in Arizona's Meteor Crater basin (Lehner et al. 2011) have been successfully simulated with a high-resolution numerical flow model (Lehner and Whiteman 2012, 2014). The removal of nighttime temperature inversions by upslope flows on the heated sidewalls and the role of compensatory sinking over the valley or basin center has been demonstrated in valleys throughout the world (e.g., Müller and Whiteman 1988; Whiteman et al. 2004; Rendòn 2014), and the roles of cross-basin and cross-valley flows and the mechanisms of basin and valley temperature inversion breakup are now summarized in several

13

textbooks and monographs (Stull 1988; Whiteman 1990, 2000; Markowski and Richardson 2010; Zardi and Whiteman 2012).

3.2 Solar radiation effects

Analyses of meteorological data from the BCM provide support for this aerosol release mechanism. In this section we will consider the solar radiation effects. We developed a solar shading algorithm to simulate movement of shadows in and around the BCM at 5-minute intervals for 21 January, the middle day of the episode. Frames from the animation were then used to create maps of the morning and afternoon shadow boundaries within the mine at hourly intervals. The boundary between shadow and sunlight progresses down the south-facing sidewall of the BCM in morning (Figure 12a) and up the south-facing sidewall in the afternoon (Figure 12b).

The north-facing sidewall typically has residual snow cover in winter, providing a source of cold air during nighttime (and much of the daytime) that brings cold air into the upper enclosed elevations of the mine. Wind data from the SAPP site, to be presented in a later section, supports this conclusion. Figure 13 is a photograph taken in December 2009 illustrating what we think is a typical wintertime snow cover difference between the north and south sidewalls produced by insolation differences. Following snowstorms, snow is soon melted off the south-facing sidewall.

3.3 Wind effects

Wind directions and speeds were not measured in the enclosed portion of the mine during the selected 15-day period. A scanning Doppler wind lidar was operated in the pit, however, during the winters of 2010-2011 and 2011-2012. This lidar provided vertical profiles of horizontal winds above the lidar location as a function of time. A cold-air pool event on 25 December 2011 (Figure 14) had very light winds within the enclosed portion of the mine during both night and day. This is typical of undisturbed cold-air pool events. The aerosol in the mine was removed following sunrise as less polluted air descended into the pit and higher aerosol content air was noted above the altitude of Bingham Pass beginning by 1100 MST and lasting through 1700 MST.

When background wind speeds are relatively high above the mine, the removal of aerosol from the mine takes place during the same time of day but is enhanced as relatively clean air and stronger winds sink into the mine volume (Figure 15). The wind speeds within the enclosed mine volume are light and variable but are more turbulent than depicted on 25 December. Much stronger winds are present at the top of the descending aerosol layer.
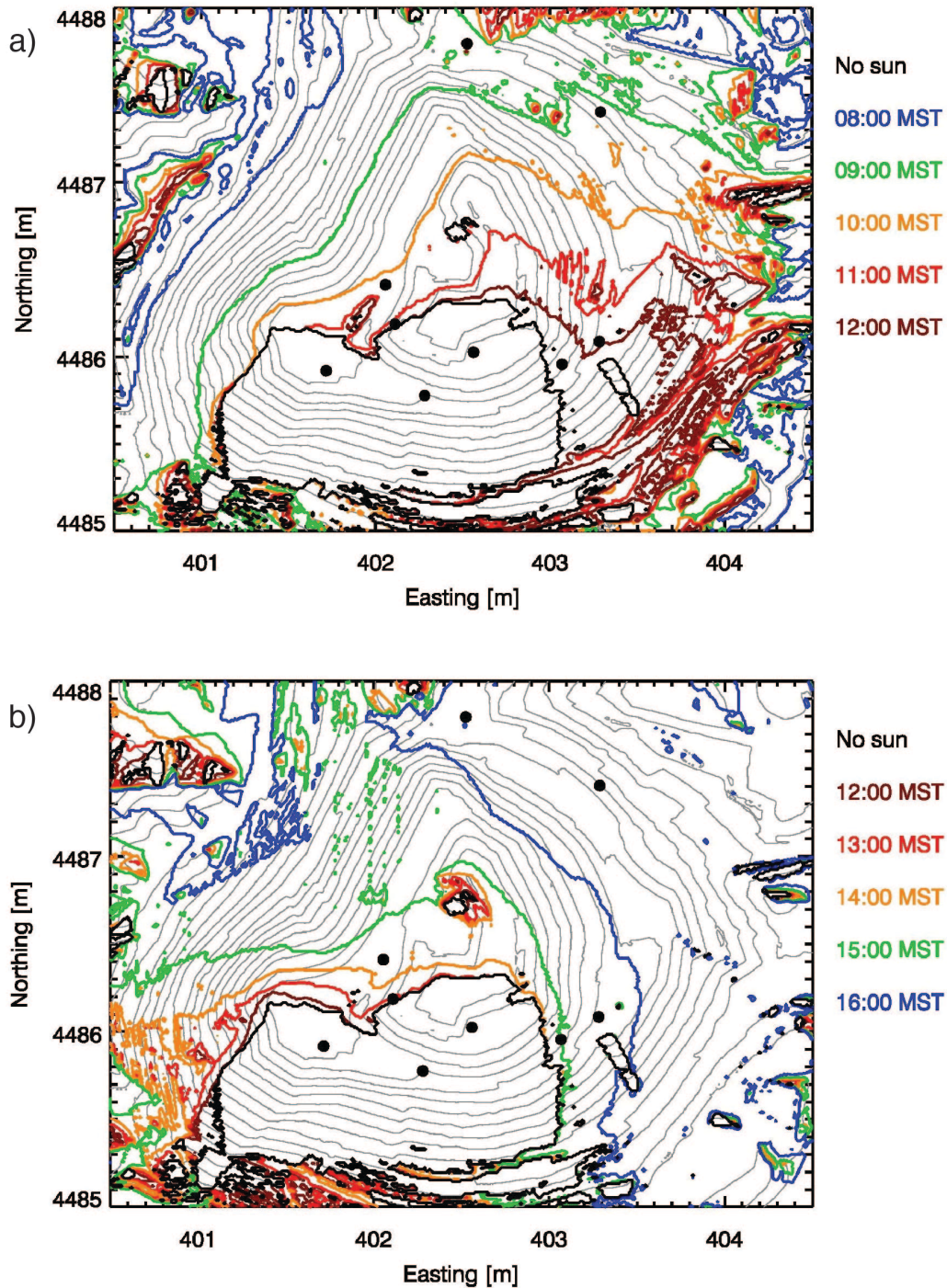
Figure 12. Isochrone analysis of shadow boundaries in the BCM for a) morning hours following astronomical sunrise (0747 MST) and b) for afternoon hours before astronomical sunset (1732 MST) on 21 January 2014. Shadow boundaries at hourly intervals are shown by the colored lines, illustrating the movement of sunlight down and back up the north face of the BCM. North is up. The lower south wall of the mine is in shadow all morning. Locations of temperature data loggers (dots) are shown for reference.

Figure 13. Aerial photograph of the BCM showing the winter distribution of snow cover in and around the mine. The view is towards the west. Photo by Michael Lynch, all rights reserved, used with permission.
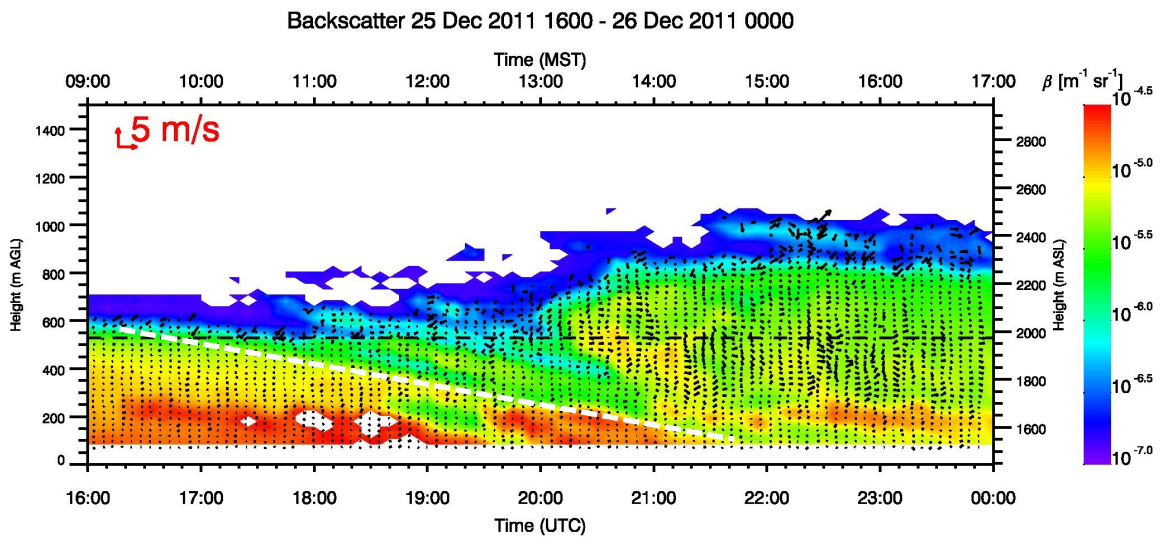

Figure 14. Time-height cross-section of Doppler lidar backscatter coefficients (colors in legend) and winds (vectors) on 25 December 2011. The dashed black line is the altitude of Bingham Pass. The dashed white line is the boundary between polluted air within BCM and the descending cleaner air from aloft.
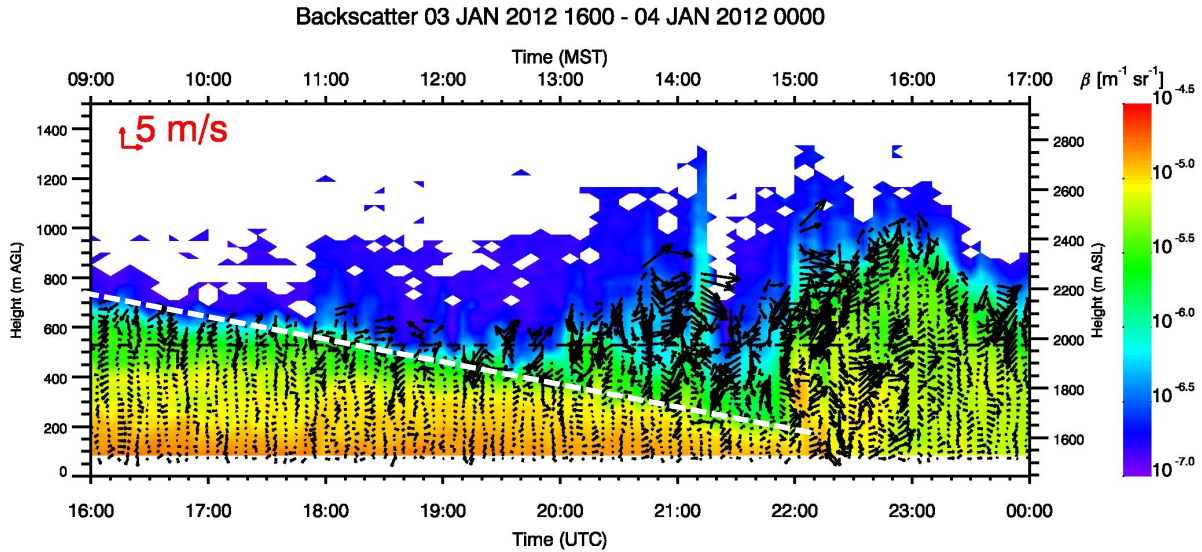
Figure 15. Same as Figure 14, except for 3 January 2012.

Figure 16 presents time series to show how changes in total aerosol mass in the mine control volume (Figure 16a) are related to changes in wind directions (Figure 16b) and speeds (Figure 16c) at the SAPP and Farnsworth Peak (FWP) sites. Farnsworth Peak at 2763 m MSL is 18 km north-northwest of BCM on the crest of the Oquirrh Mountains (see Figure 1). Aerosols being carried up the north sidewall of the mine can be expected to be observed above the enclosed portion of the mine by the aerosol lidar whenever the ambient or background flows are from a direction that transports some of the upward transported aerosol back across the pit (e.g., northwest winds). Winds were generally from the northwest during the 15-day period (Figure 16b), ensuring that the aerosols would be seen. When the wind direction at FWP changes to easterly (20, 21, 23 and 24 January) the aerosol burden in the mine decreases as some of the ventilated aerosols are apparently missed by the aerosol lidar.

The postulated drainage of cold air from the upper elevations of the pit is supported by the SAPP wind direction data. Weak downslope drainage flows from west-southwest were generally present during day and night at this site for the entire cold-pool episode except for a brief time each day during maximum insolation when winds turned briefly into an easterly upslope direction. Ambient wind speeds at the altitude of the top of the mine at SAPP (Figure 16c) are also seen to modulate the aerosol burden within the mine. Strengthening winds immediately above the mine can enhance aerosol removal and disturb the normal cycle of aerosol ventilation, as seen on 15, 22, 26 and 27 January.

Additionally, there are indications that aerosol burdens in the mine are reduced when winds become strong at FWP (Figure 16c), but this site, at an elevation of 2763 m MSL, is apparently not as representative of conditions immediately above the mine as the SAPP site during the generally low wind speed conditions associated with cold-air pools.
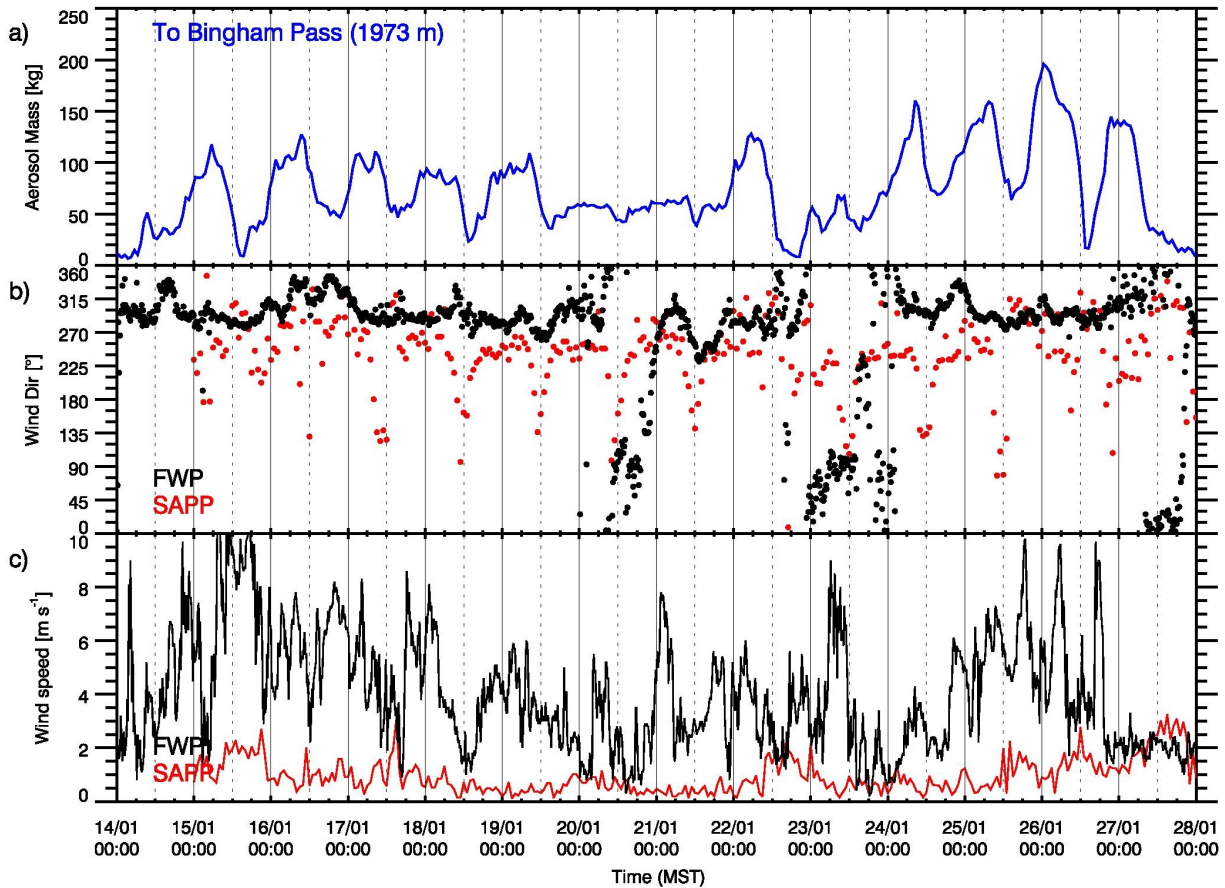
17

Figure 16. a) Volume weighted PM$_{2.5}$ aerosol mass, b) wind directions at FWP and SAPP, and c) wind speeds at FWP and SAPP during the 15-day cold-air pool episode.

3.4 Atmospheric relative humidity, temperature and stability effects

Near-surface values of relative humidity and temperature during the 14-28 January period are illustrated for the BCM and SLV ceilometer sites in Figures 17a and b. Relative humidity undergoes a regular diurnal cycle at both sites, with lowest values during the warmest time of day and highest values during nighttime. Daily maximum values typically reach over 90% at SLV, but only 75% or less in the BCM. Temperatures at the two sites range between about -8 and +9°C. Maximum temperatures are similar at both sites, with the maximum reached in early to mid-afternoon. The time of the maximum is often delayed by 1 to 3 hours in the BCM. The temperature minima are much lower in the SLV than in the BCM, as the cold-air pool there strengthens during the night.

The cycle of heating, which propagates down and up the sidewall with the shadow, changes the stability of the air within the pit, enhancing the removal of air from the mine basin and making the air in the pit more susceptible to vertical mixing into the flows aloft, especially when wind speeds aloft are strong. The winter transport of aerosols up the south-facing sidewall is
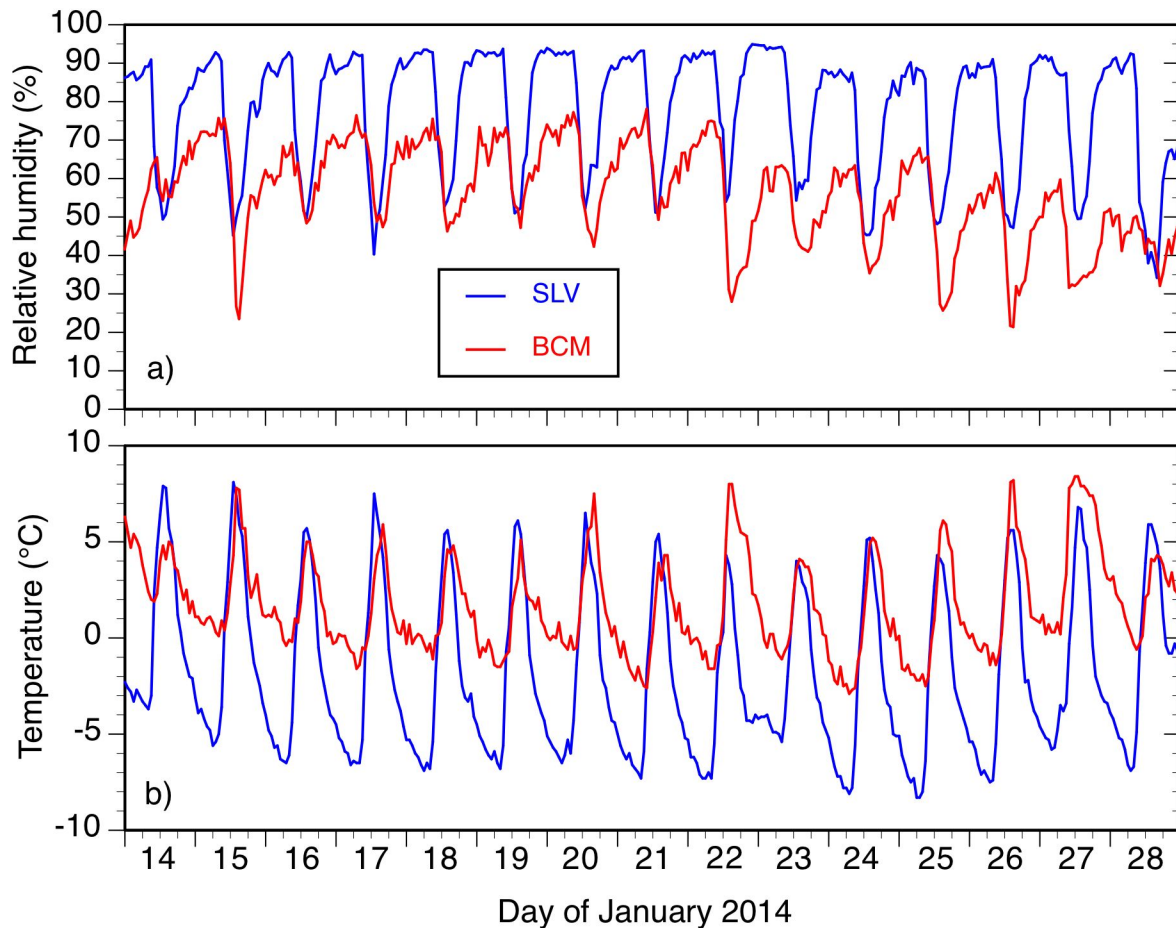
18

Figure 17. a) Relative humidity and b) temperature time series from automatic data loggers co-located with the ceilometers at 8th and 8th (blue, 1309 m MSL) and at the BCM (red, 1457 m MSL).

enhanced by weak atmospheric stability inside the pit. The mine atmosphere is stable, but is less stable than, for example, the atmosphere inside the SLV. Lower stability reduces the energy required to carry air up the heated sidewall.

Changes in atmospheric stability are produced by the diurnal cycle of temperature inversion buildup and destruction. The contemporaneous evolution of vertical temperature structure within the pit and in the adjacent SLV were observed using two lines of HOBO® automatic temperature data loggers, one inside the pit and one running down the outside of the pit to West Jordan, Utah. The uppermost temperature data logger on East Butte (see Figure 2) was common to both lines. Such *pseudo-vertical temperature profiles* from lines of surface temperature data loggers are reasonable proxies for free air temperature soundings (Whiteman and Hoch 2014). However, individual data loggers are sometimes inadvertently placed in non-representative, near-surface microclimates; these become apparent in pseudo-vertical soundings as small temperature deviations from larger scale temperature structure and are most apparent when there is little elevation difference between adjacent loggers. Temperature differences among the data loggers

are also expected to occur when some loggers are in sunlight while others are in shadow. In light wind conditions, the HOBO®s may report temperatures that are too high when in direct sunlight, despite the sensor's exposure in a naturally ventilated solar radiation shield (Whiteman et al. 2000).

Changes in atmospheric stability within the pit are driven primarily by progression of solar radiation up and down the north sidewall. But, radiative interactions among the sidewalls are also expected to affect air temperatures and temperature structure within the basin volume (Hoch et al. 2010; Hoch et al. 2011), although we have not yet specifically evaluated this for the BCM.

To evaluate changes of temperature structure and atmospheric stability inside and outside of the mine basin, we have taken the approach of compositing pseudo-vertical temperature sounding data from four representative days (16, 17, 18 and 19 January 2014) with similar temperatures and temperature structure evolutions and similar diurnal cycles of aerosol backscatter. Mean hourly soundings are shown, as computed from 5-min observations. We present composite day data for both BCM and SLV, breaking the soundings into nighttime cooling and daytime warming periods.

A. SALT LAKE VALLEY

The evolution of the SLV temperature structure is shown in Figure 18. During the cooling period (Figure 18a) the structure evolved from a convective layer that extended to 1800 m MSL in late afternoon to a strong nighttime inversion that extended to 1900 m MSL, with an isothermal or weak stability layer above. An urban heat island, with a dry adiabatic lapse rate (i.e., lapse rate parallel to the dot-dash curve), was present within the city of West Jordan extending to an elevation of about 1500 m MSL. During the warming period (Figure 18b) the temperature structure evolves back into the afternoon convective regime, which is capped by a deeper elevated temperature inversion. During this evolution, the top of the nighttime temperature inversion sinks into the valley, warming the valley atmosphere through subsidence and horizontal heat flux convergence. The urban heat island is destroyed by the upward growth of convection from the heated ground.

B. BINGHAM CANYON MINE

The temperature structure evolution within the Bingham Mine (Figure 19) is much more regular than the structure in the wider SLV, which is open to a broader range of meteorological influences (along-valley thermally driven circulations, outflows from tributaries, influences from the Great Salt Lake, and from larger-scale ambient flows aloft). In late afternoon the temperature structure in the BCM is composed of four stacked layers. A very strong temperature inversion is present at the mine floor. This inversion is enhanced by a microclimate in the neighborhood of the lowest elevation data logger, a small sub-basin on the mine floor that was not illuminated at all during daytime. Thus, the diurnal temperature range at this logger is small. The second layer is a stable layer extending from 1500 to 1800 m MSL. This is surmounted by a near-neutral or super-adiabatic layer, which extends to 1950 m MSL. The fourth layer is an elevated inversion
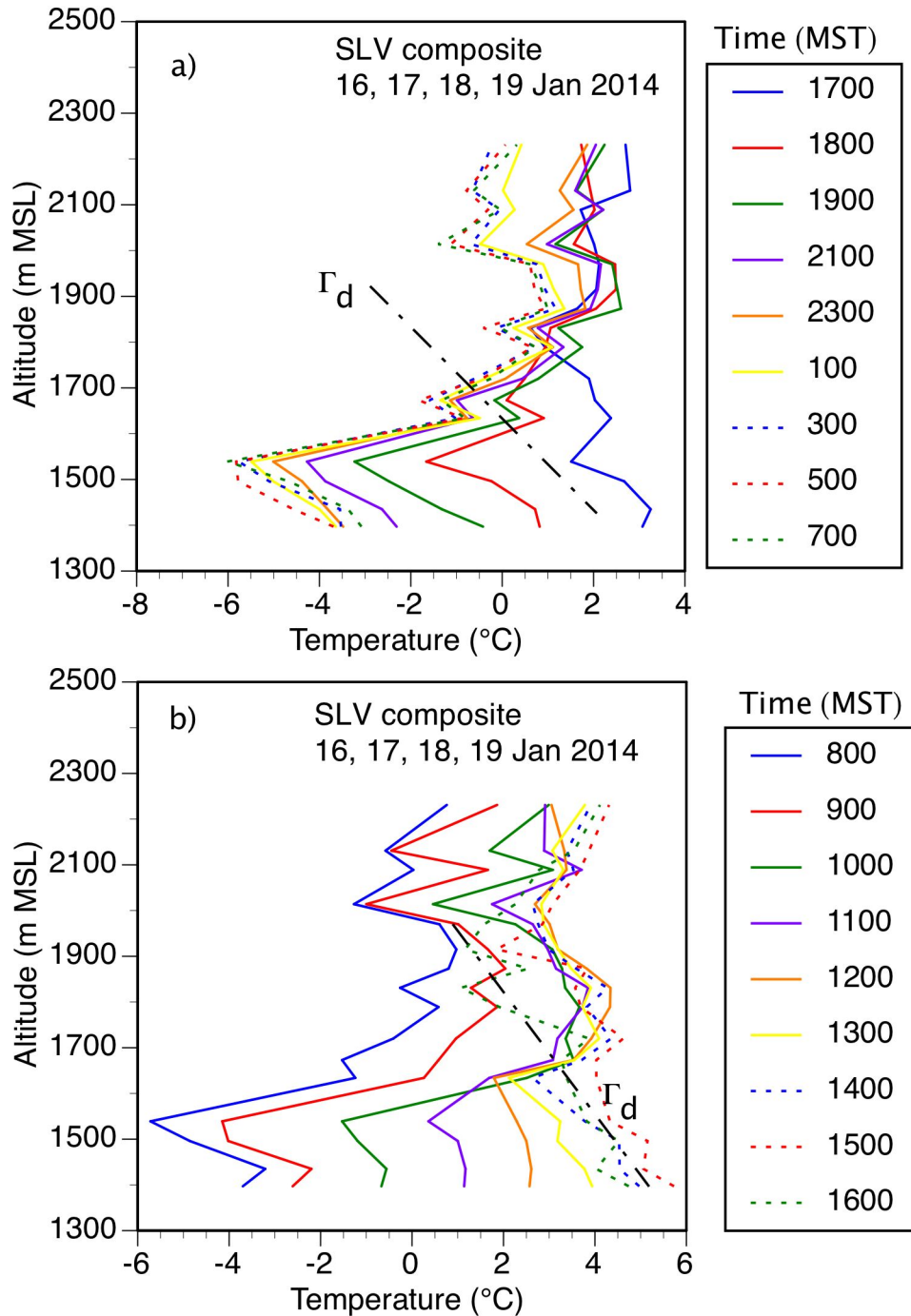
Figure 18. Hourly pseudo-vertical temperature soundings from the HOBO® line outside the BCM in the Salt Lake Valley a) during the cooling (1800 to 0800 MST) and b) warming (0900 to 1700 MST) periods of a mean day. The mean day shown is a composite of 16, 17, 18, and 19 January 2014. The times indicated are the ending times of the 1-h averages. Shown, for comparison, is the dry adiabatic lapse rate of 9.8°C/km.

layer, which extends from Bingham Pass to East Butte. The third, super-adiabatic layer is indicative of a flow of cold air coming down the sidewall from the winter snow cover in the upper mine basin. Evidence for this flow is seen in data from the KUC-operated automatic weather station SAPP (Figure 16). Similar temperature structures were observed in Arizona's Meteor Crater basin (Whiteman et al. 2010; Adler et al. 2012) when a mesoscale cold-air drainage flow intruded into the crater basin over the southwest rim, and in the Grand Canyon of the Colorado River (Whiteman et al. 1999), which experiences a neutral atmosphere both night and day that is thought to be produced by the continuous drainage of cold air off the elevated winter snowpack on the canyon's North and South Rims. The fourth layer senses the larger-scale temperature inversion in the upper elevations of the SLV.

The strong inversion on the mine floor is present all night, with its strongest stability in late afternoon (Figure 19a). The elevated inversion between East Butte and Bingham Pass is present all night, with stability strongest near sunrise. The upper half of the pit maintains its super-adiabatic profile all night (and during the day) caused by the continuous flow of cold air into the pit from the snow-covered upper portions of the mine, which lose heat by longwave emission to the sky. This import of cold air into the pit causes overturning and mixing in the upper portions of the pit. A similar, but shallower, super-adiabatic layer is seen in the SLV profiles (but not in the free air in the main valley, see Appendix B), indicating that a source of cold air is also generated on the outer slope of the mine by residual snow cover on East Butte. The pit cools very uniformly during the night while maintaining its four-layer structure. The temperature on the mine floor remains nearly constant during the night, with the highest rate of cooling occurring in the second layer, but with cooling also being prominent in the third and fourth layers.

The temperature structure in the mine changes relatively quickly during daytime (Figure 19b) when insolation provides a source of heat on the mine's south-facing sidewall. The maximum rate of warming between adjacent hourly soundings is seen to progress deeper and deeper into the mine during the morning and early afternoon, although retreating in the late afternoon. The top of the mine inversion is also seen to sink into the mine during the day. The heating of the mine atmosphere, as for the SLV atmosphere, is caused partly by sinking of potentially warmer air into the mine in response to airflow up the heated sidewall, and partly by horizontal heat flux convergence. The black dotted lines in Figure 19b mark the upper and lower boundaries of the elevated stable layer that maintains its stability during descent. Unlike the SLV, convection from the mine floor plays a minor role, as only parts of it are illuminated, and then for only a small part of the day.

The atmosphere inside the BCM is generally warmer than the atmosphere in the adjacent SLV (Figure 20). During the nighttime or cooling period (Figure 20a) it is up to 8 or 9°C warmer inside the pit at elevations below 1800 m MSL than in the adjacent SLV. Between 1800 and 2100 m MSL, the atmosphere inside the pit is cooler than at the same elevation outside the mine. This is caused by cold air over the snowpack at elevations at and above Bingham Pass. Drainage of the cold air into the mine overturns air in the upper pit producing a well-mixed or neutral atmosphere. Detrainment of cold air as it comes down the sidewalls is responsible for the super-adiabatic temperature profiles there and the relatively warm air in the upper part of the mine. During the heating part of the daily cycle (Figure 20b) the temperature differences are
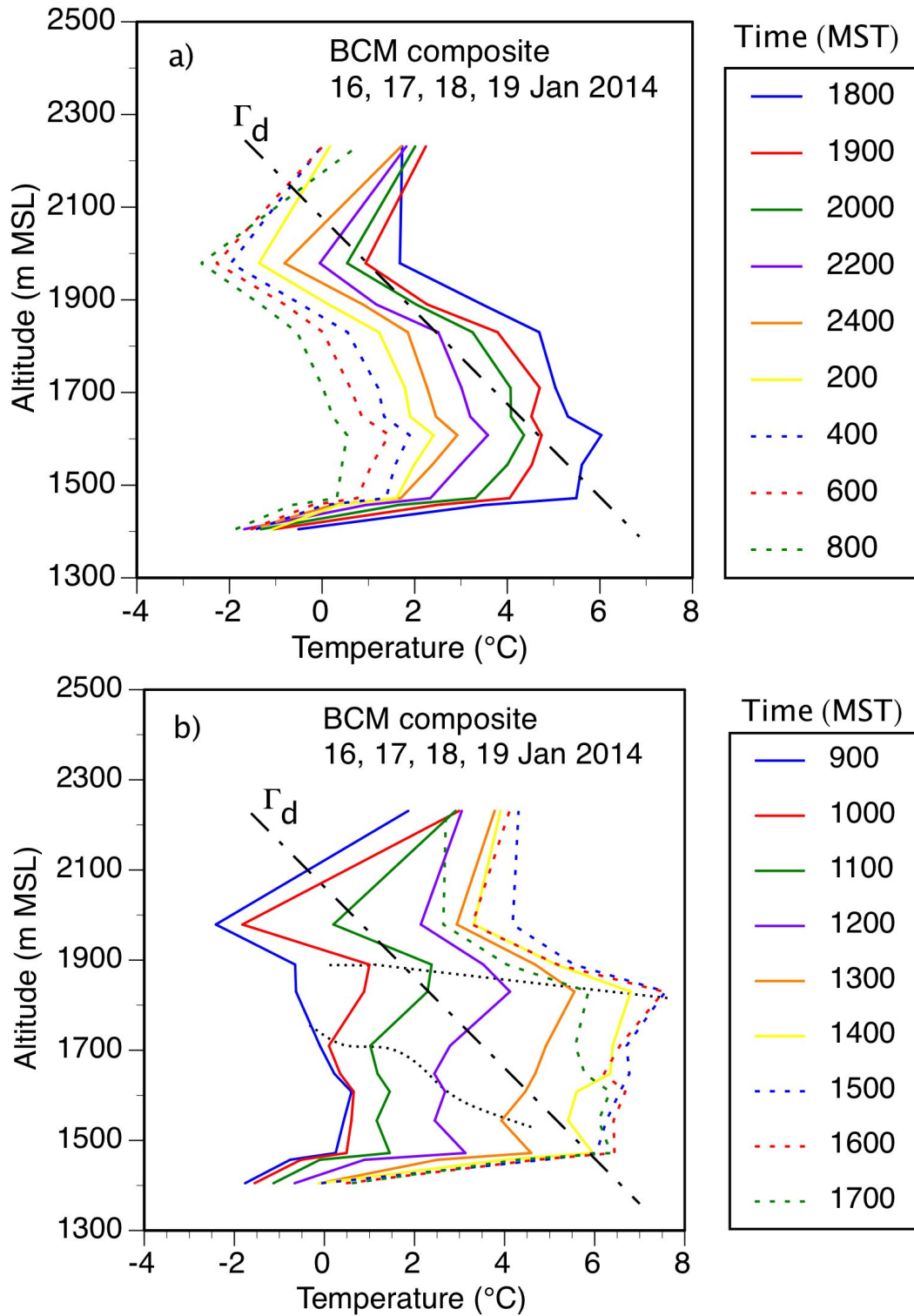
Figure 19. Same as Figure 18, but for the BCM HOBO® line. The two black dotted lines delineate the upper and lower boundaries of a constant stability layer that descends into the mine, warming the mine atmosphere.
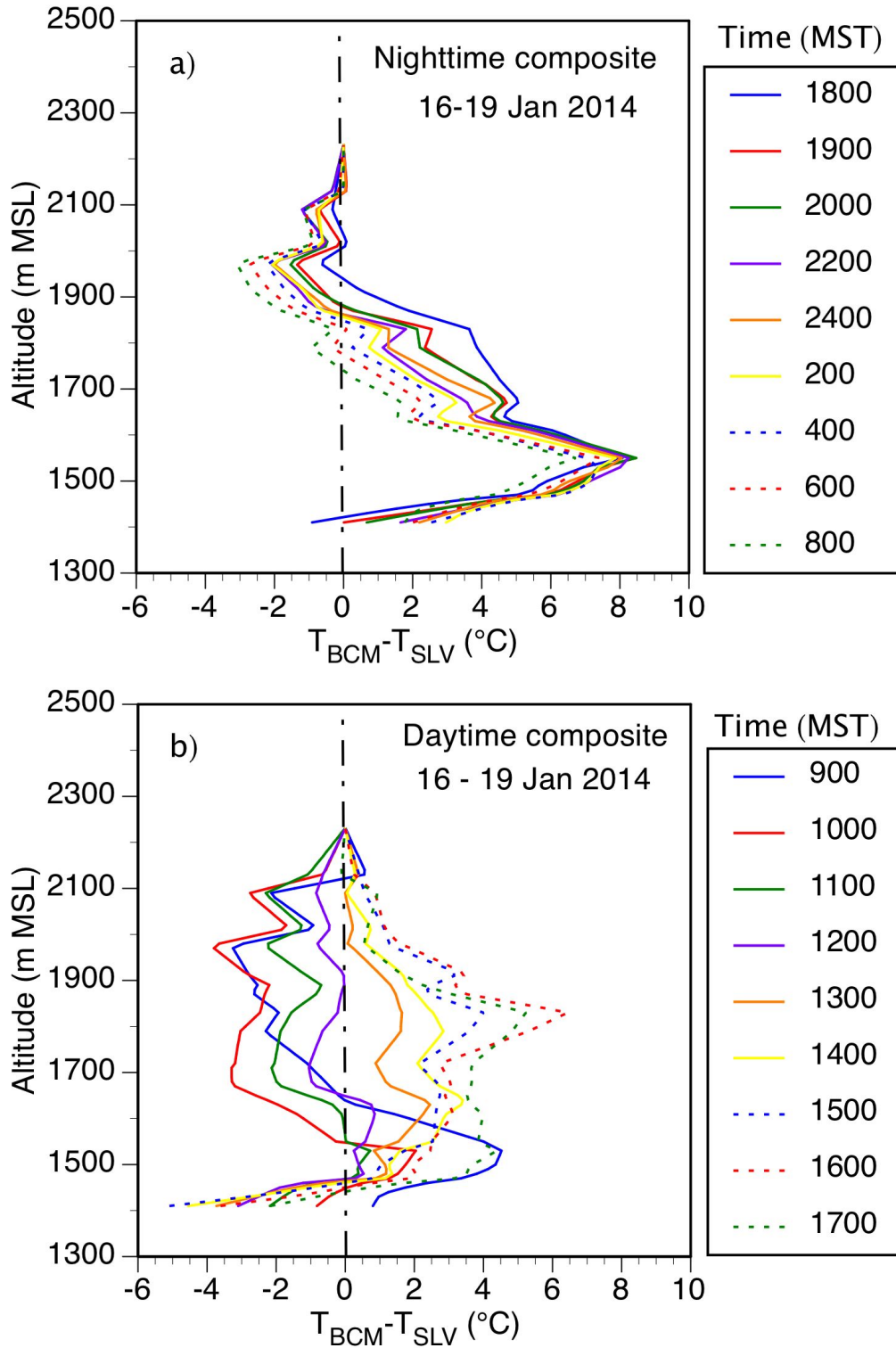
Figure 20. Temperature differences (T_{BCM}-T_{SLC}) as a function of altitude between the BCM and SLV HOBO® lines during a) the cooling and b) warming periods of the mean winter day composited from data for 16, 17, 18 and 19 January 2014.

more variable with altitude and the rate of heating during the 9-hour heating period is greater than the rate of cooling during the 15-hour cooling period.

This excess warmth in the Bingham Mine is unusual for a high altitude basin, as other high altitude basins throughout the Western United States and Europe are generally reservoirs of cold air and even hold minimum temperature records (e.g. Peter Sinks in northern Utah holds a minimum temperature record of -56.3°C). We think this relative warmth is caused by the lack of exposure of the surfaces in the mine to the cold radiating sky (i.e., a low sky-view fraction). Additionally, the longwave radiative transfer within the mine is much like a blackbody cavity in which temperatures are driven toward isothermalcy. There is also some anthropogenic heat released in the mine by blasting and by internal combustion in haul vehicles, generators, and other mine machinery. Our initial calculations suggest that the anthropogenic heat release (1/8 K hr^{-1}), while significant, is relatively minor.

Of special importance to air pollution investigations is the strong stability that is present in the Salt Lake Valley below the mine during cold-air pool episodes. Air leaving the mine would have to be cooled significantly to reach temperature equilibrium with air already present on the valley floor. Air leaving the mine would gain nearly 8°C by adiabatic compression as it descended the ~800 m between the mine exit and the valley floor. This thermodynamic warming can be calculated from $\Delta T = 800 \cdot \Gamma_d$ where $\Gamma_d = 0.0098°C/m$. Considering the temperature of air parcels leaving the mine during both day and night and the contemporaneous minimum temperatures at or just above the valley floor, we see that parcels leaving the mine would need between 7.5 and 12°C of cooling to reach an equilibrium with air already on the valley floor. Because this amount of cooling is quite unlikely, the aerosols leaving the mine are not expected to contribute to air pollution problems on the floor of the Salt Lake Valley when typical winter cold-air pools are present there.

The availability of BCM aerosol backscatter data and the knowledge of the meteorological mechanisms leading to aerosol ventilation from the mine suggests a method, hitherto unexplored, to estimate the ventilation of aerosols from the mine. In the next sections this method will be developed mathematically and applied to the Bingham Canyon Mine.

4. Estimation of volume-weighted aerosol mass in the mine volume

The aerosol mass in the BCM atmosphere could be estimated if a relationship could be found between the measured aerosol backscatter and PM$_{2.5}$ and PM$_{10}$ concentrations. We performed a literature survey to find peer-reviewed technical papers that provide insight into this relationship, finding several relevant papers (Gan et al. 2011; Münkel et al., 2003, 2004, 2007). To make our investigations more representative of local conditions, however, we developed regression relationships between hourly PM$_{2.5}$ (Figure 21a) and PM$_{10}$ (Figure 21b) concentrations measured by UDAQ at Hawthorne Elementary School and hourly aerosol backscatter coefficients from our 8th and 8th ceilometer. The CL31's fourth range gate (30-40 m elevation) is the first suitable range gate for this comparison. Despite the 2-km distance between the ceilometer and Hawthorne sites and the use of a range gate that is 30-40 m above ground, good regression relationships were found, consistent with those found by other investigators in our literature survey. The

regression relationships are a function of relative humidity, a feature known from other investigators. Because relative humidity in the BCM was generally below 75% (Figure 17a), we developed regression relationships for $PM_{2.5}$ (Figure 22a) and PM_{10} (Figure 22b) and aerosol backscatter at the Hawthorne site (Figure 10a) for relative humidities below 75%, after omitting the high backscatter values from low clouds on the night of 22-23 January.
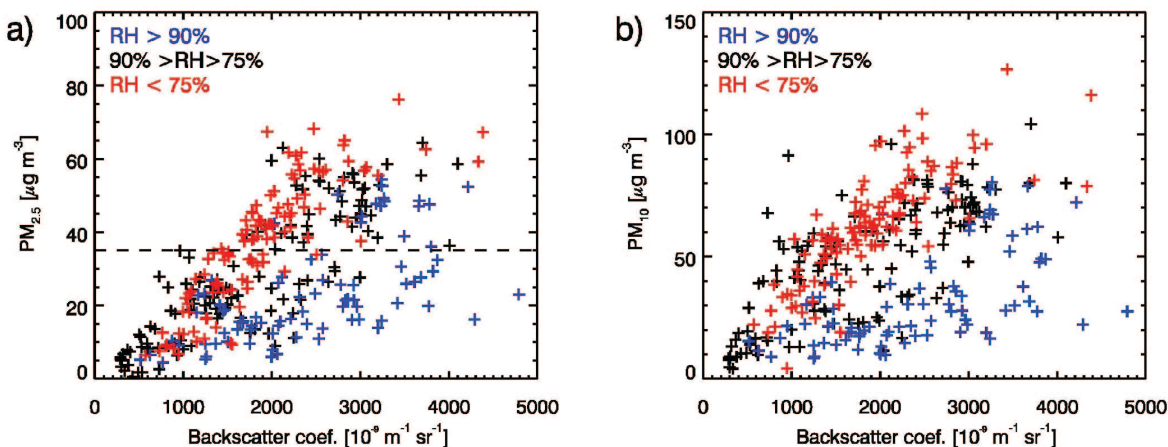

Figure 21. Hourly a) $PM_{2.5}$ and b) PM_{10} concentrations at Hawthorne Elementary School versus hourly ceilometer backscatter coefficient (30-40 m height) at the 8th and 8th site for the 14 - 28 January 2014 period. Symbols indicate different ranges of relative humidity (RH), where red symbols are for RH ≤ 75%, blue for 75 < RH < 90% and black for RH ≥ 90%. The 24-h-avg NAAQS for $PM_{2.5}$ (PM_{10}) is 35 (150) μg m^{-3}.
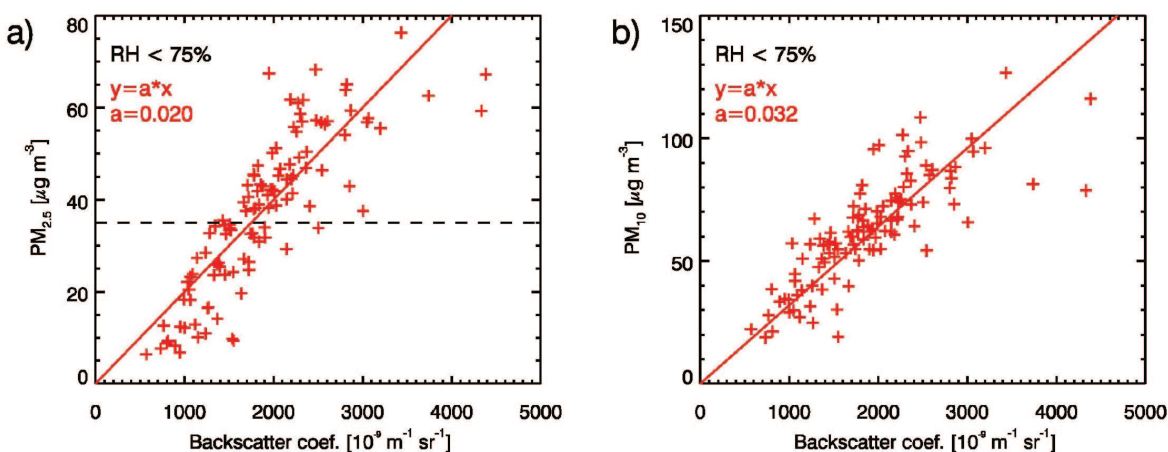

Figure 22. Regression of a) $PM_{2.5}$ and b) PM_{10} concentration versus backscatter coefficient for humidity below 75%. The dashed line shows the 24-h-avg NAAQS for $PM_{2.5}$.

The linear backscatter-PM$_{2.5}$ and backscatter-PM$_{10}$ relationships determined from data collected in the SLV were then used to convert the BCM backscatter data to *equivalent* PM$_{2.5}$ (Figure 23a) and PM$_{10}$ (Figure 23b) aerosol concentrations. *Equivalent concentrations* may differ from true concentrations, as the type of aerosols and their scattering characteristics may differ between the Hawthorne and BCM sites. The resulting equivalent concentration isopleths are numerically identical to the Figure 10 isopleths of backscatter coefficient but they are reported in Figure 23 on a linear scale rather than a logarithmic scale. The highest equivalent concentrations of PM$_{2.5}$ (up to 350 μg m^{-3}) occur near the mine floor around sunrise. Equivalent concentrations in the range of 50 - 100 μg m^{-3} are fairly well distributed vertically in the lowest 350 m of the BCM. ***These equivalent concentration estimates are based on the assumption that the aerosols in the mine are of the same size and composition as those in the SLV and thus have the same scattering properties. Only co-located observations of backscatter and PM$_{2.5}$ and PM$_{10}$ concentrations could validate this assumption.*** Comparisons between co-located BCM and SLC ceilometers were made both before and after the cold-pool episode, with nearly identical backscatter results, providing confidence that the ceilometers were operating identically.
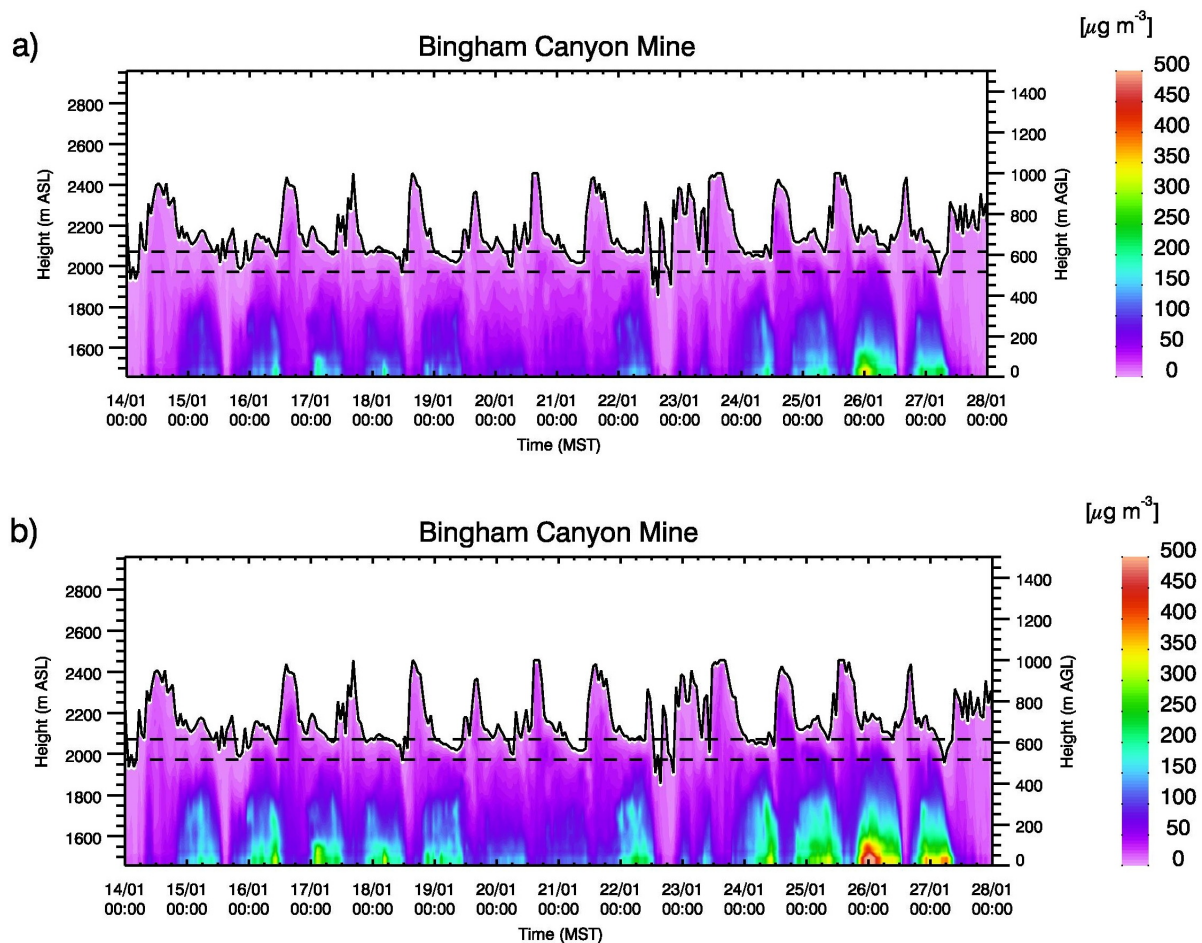

Figure 23. Equivalent a) PM$_{2.5}$ and b) PM$_{10}$ concentrations (μg m^{-3}) as a function of time and height in the BCM for the 15-day period.

The regression equation used to estimate equivalent PM$_{2.5}$ concentration for RH $\leq$ 75% is:

$$\chi_{PM2.5} = -0.005 + 0.020 \text{ x } 10^9 \text{ m sr} * \beta \quad [\mu g \text{ m}^{-3}] \tag{1}$$

where the volume backscatter coefficient β is in m^{-1} sr^{-1}. The correlation coefficient is r = 0.83 and the root mean square error is 11.6 μg m^{-3}.

The regression equation used to estimate equivalent PM$_{10}$ concentration for RH $\leq$ 75% is:

$$\chi_{PM10} = 16.09 + 0.0247 \text{ x } 10^9 \text{ m sr} * \beta \quad [\mu g \text{ m}^{-3}] \tag{2}$$

with a correlation coefficient of r = 0.80. If the regression curve is constrained to pass through the origin, the regression equation becomes

$$\chi_{PM10} = 0.032 \text{ x } 10^9 \text{ m sr} * \beta \quad [\mu g \text{ m}^{-3}] \tag{3}$$

and the root mean square error is 14.0 μg m^{-3}.

Aerosols were assumed to be horizontally homogeneous within the mine, varying only with altitude. The total equivalent aerosol mass within the mine to the elevation of Bingham Pass was then calculated by weighting the equivalent concentration profiles by the drainage area of the pit (see Figure 4) using the equation:

$$M(t) = \int_{Mine \, floor}^{Bingham \, Pass} \chi(z,t) \, A_H(z) \, dz \quad [kg] \tag{4}$$

where $\chi(z,t)$ is equivalent aerosol concentration (whether PM$_{2.5}$ or PM$_{10}$), A_H is drainage area and z is height. The integration interval is 10 m and concentration between 30 m above the ceilometer and the BCM floor are assumed to be equal to the equivalent concentration estimated from the backscatter at the lowest range gate with good backscatter data. The time series of total equivalent aerosol mass $M(t)$ in the enclosed mine between the mine floor and the ceilometer, between the mine floor and Bingham Pass and between the mine floor and the East Ridge were calculated and are shown in Figure 24. Note that the contribution of aerosol mass from below the ceilometer (calculated from concentration estimates using the first valid backscatter reading) does little to affect the total mass in the mine since the volume weighting is small at the lower altitudes. Total equivalent PM$_{2.5}$ (PM$_{10}$) aerosol mass within the mine basin during the 14-28 January period generally varied between 10 and 200 kg (20 and 350 kg). A regular diurnal cycle is apparent, with aerosol mass building up within the pit from late afternoon to about 0900 MST and with the mass decreasing rapidly between 0900 MST and late afternoon.

Note that the time series of PM$_{10}$ aerosol mass has different numerical values than the corresponding PM$_{2.5}$ curve, but has exactly the same shape. The volume-weighted equivalent aerosol masses in Figure 24 are the sum of mass contributions from each of the 10-m-deep layers. Figure 25 shows the volume-weighted equivalent mass for PM$_{2.5}$ for the individual 10-m-deep layers as a function of height. A PM$_{10}$ figure would look just the same, but with different
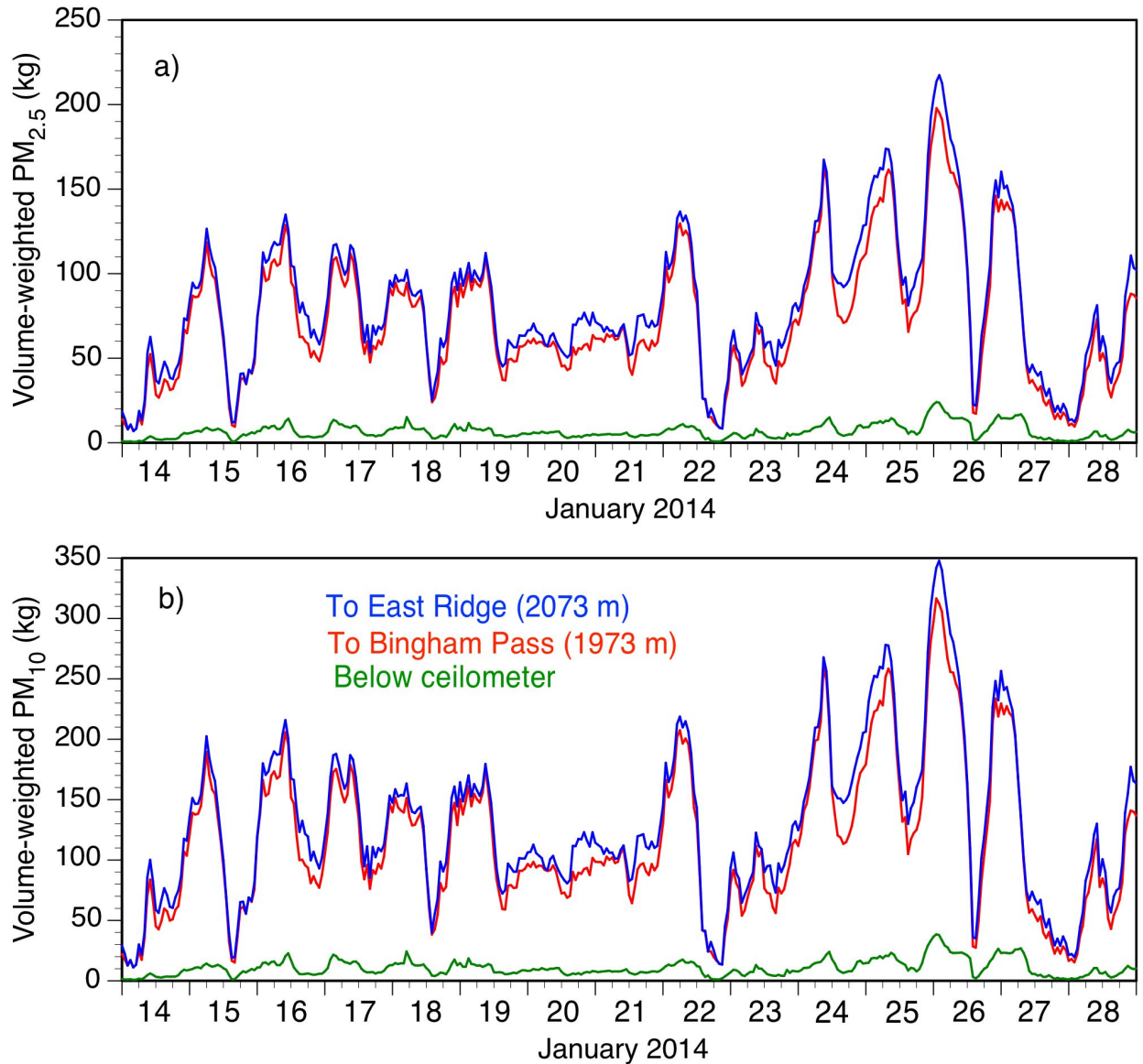
Figure 24. Time series of total equivalent a) $PM_{2.5}$ and b) PM_{10} atmospheric aerosol mass totals M (kg) within the enclosed portion of the BCM below the elevation of the ceilometer (1457 m MSL), below Bingham Pass (1973 m MSL) and below East Ridge (2073 m MSL).

numerical values. On many days the peak mass is found near the altitude of the crusher, where the haul trucks congregate. However, the mass is, overall, fairly evenly distributed with elevation from the mine floor to altitudes just below the elevation of Bingham Pass. The mine drainage area increases rapidly at altitudes above Bingham Pass and the equivalent particulate mass there is clearly over-emphasized by the volume weighting, suggesting that the particulates seen by the ceilometer over the mine center at these altitudes are not distributed uniformly across the mine width.
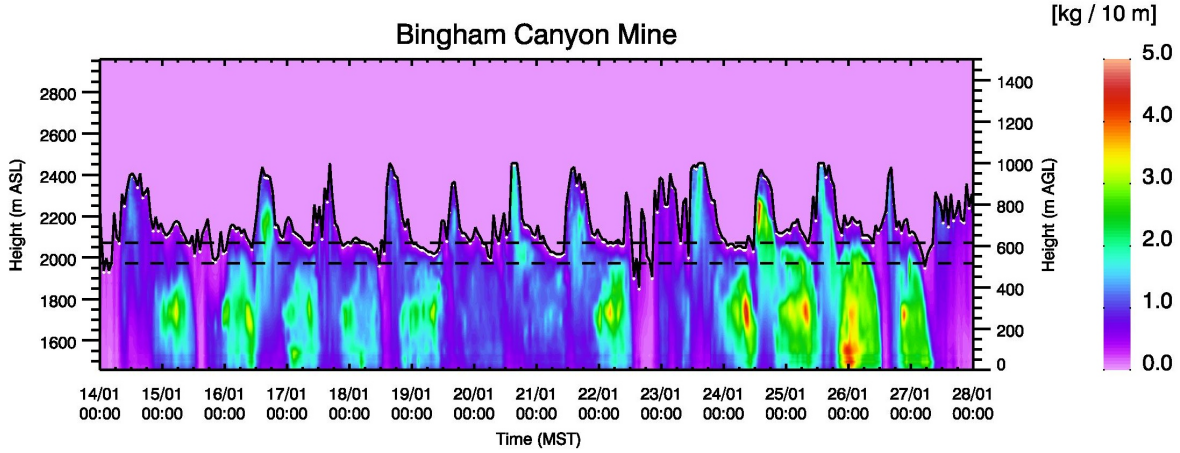
Figure 25. Time-height plot of volume-weighted equivalent PM$_{2.5}$ aerosol mass per 10-m-deep layer.

5. Mathematical model

The diurnal changes in aerosol mass suggest a new method for estimating aerosol ventilation from the mine, as increases or decreases of aerosol mass with time in the mine volume are related to sources and sinks of aerosol mass. The total rate of change of aerosol mass within the enclosed BCM atmosphere is given by

$$\left.\frac{dM}{dt}\right]_{storage} = \left.\frac{dM}{dt}\right]_{emission} + \left.\frac{dM}{dt}\right]_{chem} - \left.\frac{dM}{dt}\right]_{deposition} - \left.\frac{dM}{dt}\right]_{ventilation} \qquad (5)$$

where the terms are 1) the rate of increase of aerosol mass storage in the mine control volume, 2) the rate of increase of aerosol mass within the volume due to primary particulate emissions, 3) the rate of increase of aerosol mass within the volume due to chemical conversions of gaseous precursors to secondary particulates, 4) the rate of decrease of aerosol mass within the volume due to particulate deposition, and 5) the rate of decrease of aerosol mass within the volume caused by particulate escape out the top of the volume. Term 3 is intended to include all forms of deposition, including sedimentation.

Terms 2, 3, and 4 can be grouped together to define the "effective rate of emission", as follows:

$$\left.\frac{dM}{dt}\right]_{eff} = \left.\frac{dM}{dt}\right]_{emission} + \left.\frac{dM}{dt}\right]_{chem} - \left.\frac{dM}{dt}\right]_{deposition} \qquad (6)$$

so that (3) becomes:

30

$$\frac{dM}{dt} = \frac{dM}{dt}\bigg]_{eff} - \frac{dM}{dt}\bigg]_{ventilation} \qquad\qquad (7)$$

Thus, the rate of change of aerosol mass within the mine can come about due to changes in the effective emission rate within the mine and/or the rate of ventilation of material out the top of the mine. The governing rate equation (5) can be integrated with respect to time to compute daily values of the individual terms. Ratios of the daily values of the individual terms are useful for visualizing their relative importance.

6. Particulate emissions and storage rates in the mine control volume

Because there are no data on chemical conversion rates that may lead to secondary particulate formation in the mine our calculations will be limited to primary particulates. Neglecting chemical conversions is expected to be more appropriate for PM_{10} than for $PM_{2.5}$, since the particles produced by chemical reactions of precursor gases in the atmosphere tend to be in the smaller size ranges, adding relatively more mass to the $PM_{2.5}$ fraction than to the PM_{10} fraction. Thus the 3rd term of (5) is assumed negligible.

For convenience we will designate the terms in the rate equations as S, E, D and V for rates of storage, emission, deposition, and ventilation, respectively, so that (5) becomes S = E - D - V.

6.1. Primary particulate emission rates within the BCM control volume

Daily total emissions of primary particulates from the mine are reported by KUC to UDAQ using prescribed methods. Emission values are provided for all sources within a "Pit Influence Boundary" (PIB, Figure 26) including roadway fugitive dust, generators, blasting, crushing, loading, vehicle emissions, etc. Emission estimates are obtained using EPA emission factors (US EPA 2008) and the methodology described in the NONROAD modeling guidance for tailpipe emissions (EPA 2004a and b), given vehicle miles traveled, tonnage hauled, diesel fuel usage, etc. For our mathematical model it was necessary to multiply the reported daily emissions values (tons per day) by a factor of 5 to account for the fact that only 20% of the emissions were reported because a release fraction of 20% had been applied, to reduce the daily emission rates by a factor of 0.6 to account for our smaller control volume (area delineated by the black line in Figure 26), and by a factor of 907.185 to convert the daily emission estimates from English (tons) to metric (kg) units. The 0.6 factor is a rough estimate based on the ratio of the areas of the PIB and control volume (after accounting for the lack of mining sources on the south through northwest upper sidewalls of the mine) and monthly haul road traffic; some of this traffic carries waste rock to dump sites outside our control volume and some of the mining occurs above our control volume. With further effort this estimate could be improved. In future, the continuously recorded GPS readings from the haul trucks could be used to make even better estimates. The GPS data were not available for the period in question, as they are usually discarded after a certain passage of time in favor of monthly data.

No estimates are available for secondary particulate emissions that would be produced by in-pit chemical conversions of precursor gases. Additionally there are no historical or current

measurements of ambient levels of $PM_{2.5}$ and PM_{10} concentrations within the pit (Kristensen 2014, personal communication).

Daily emissions during the 15-day episode (Figure 27) were relatively uniform, with a $PM_{2.5}$ mean and standard deviation of 444 ± 69 kg/day and a PM_{10} mean and standard deviation of 3959 ± 537 kg/day. There is also little variation in emission rates within a day, as mining activity is relatively uniform from shift to shift (Kristensen 2014, personal communication). On this basis we assume that mining emissions are evenly distributed through 24-hour periods, but vary somewhat from day to day.
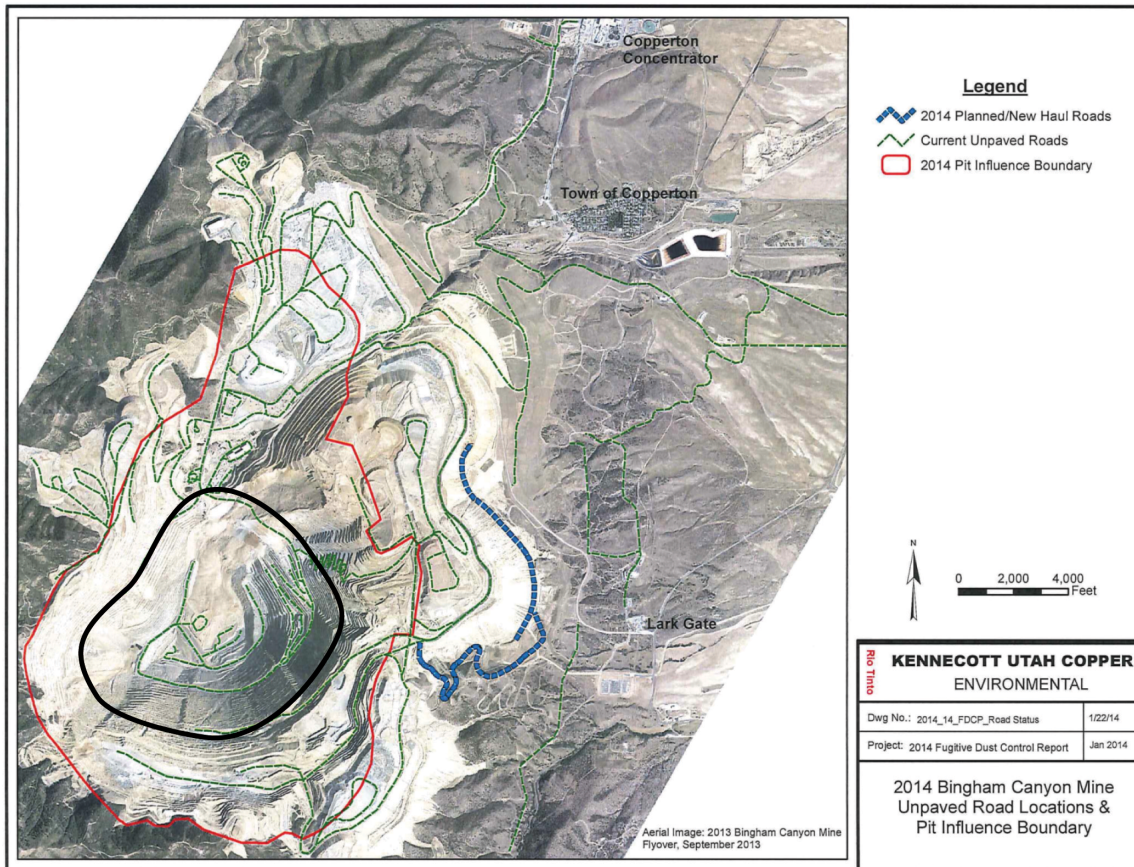

Figure 26. The BCM daily emissions data provided by KUC reports all sources of primary $PM_{2.5}$ and PM_{10} inside the Pit Influence Boundary (red curve). The control volume for our escape calculations (black curve) is a smaller area.
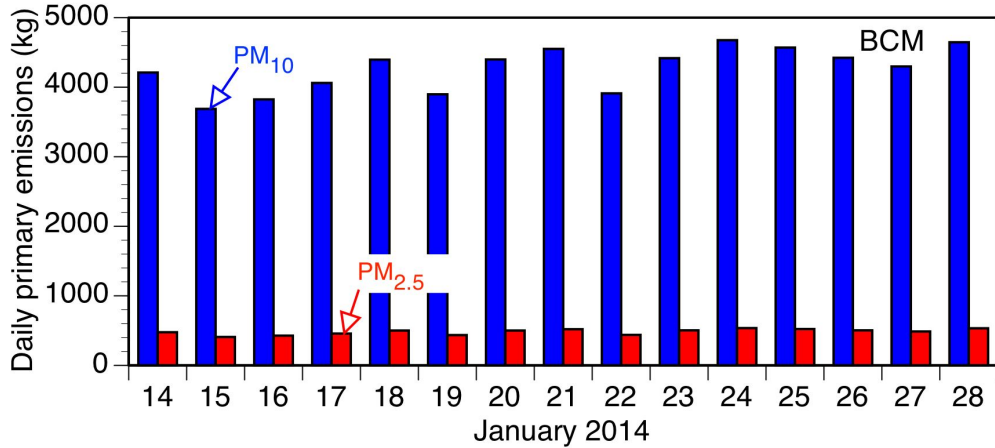
Figure 27. Daily primary in-pit $PM_{2.5}$ and PM_{10} emission estimates for the control volume obtained by converting from short tons to kg (factor of 907.185), accounting for the smaller control volume compared to the PIB (factor of 0.6) and compensating for the application of a 20% release fraction to the reported emissions (by multiplying by 5).

6.2. Particulate mass storage rates within the BCM control volume

The airborne equivalent particulate mass stored in the mine control volume, as determined by weighting the ceilometer's vertical concentration profile with the mine volume, varied with time during the cold-pool episode (Figure 28), with typical aerosol loadings of 20-300 kg. Aerosols build up overnight, reaching a maximum value shortly after sunrise. The aerosols in the mine atmosphere then decrease through the day reaching a minimum value in late afternoon. This pattern is repeated on successive days.
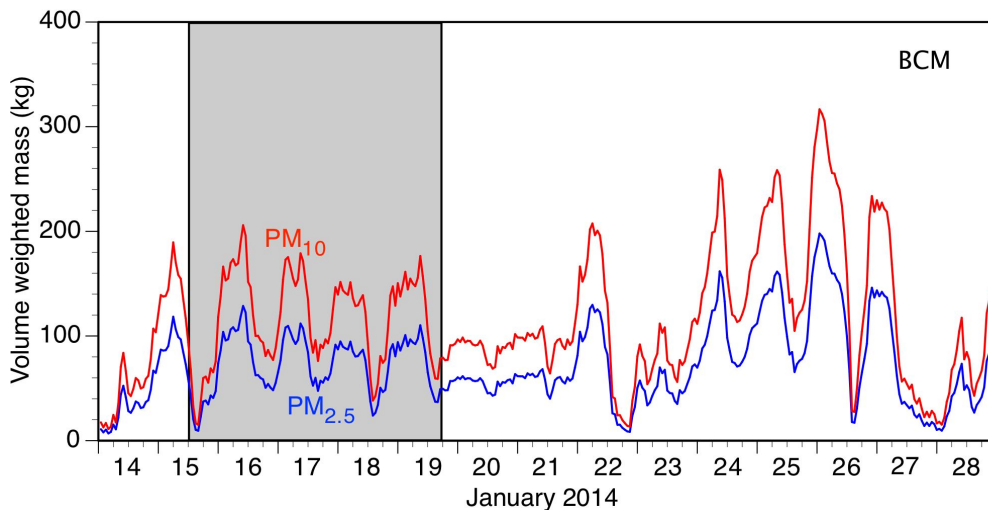

Figure 28. Equivalent particulate mass in the atmosphere of the BCM control volume (below the elevation of Bingham Pass, 1973 m MSL) as a function of time for the entire 15-day episode. The shaded area is the period composited to produce a 'typical' composite day.

6.3. Relationship between atmospheric stability and equivalent aerosol loading in the BCM atmosphere

Now that we have a curve for the volume-weighted particulate mass, we can evaluate the effects of stability changes on this quantity, finding that the lowering of stability inside the mine is, naturally, closely tied to the timing of aerosol release (**Figure 29**). For this comparison we use the *heat deficit* as an integrative measure of atmospheric stability, calculated as:

$$H(t) = \rho \, c_p \, \int_{z_0}^{z_1} [\theta(z_1, t) - \theta(z, t)] \, dz \qquad (9)$$

where z_0 = 1500 m MSL, z_1 = 1950 m MSL is the elevation near Bingham Pass and $\theta(z, t)$ are hourly pseudo-vertical potential temperature soundings from the automatic temperature loggers in the pit. The integration is not started from the mine floor, since there is little change in temperature from day to night there because it remains in shadow. Large positive values of H correspond to high stability in the pit; small values correspond to weak stability and negative values correspond to instability. The release of aerosols from the BCM is closely related to decreases of stability (increases in instability) in the mine atmosphere associated with the solar heating of the south-facing sidewall. As expected, an increase in instability is closely related to the diurnal ventilation of $PM_{2.5}$ from the mine.
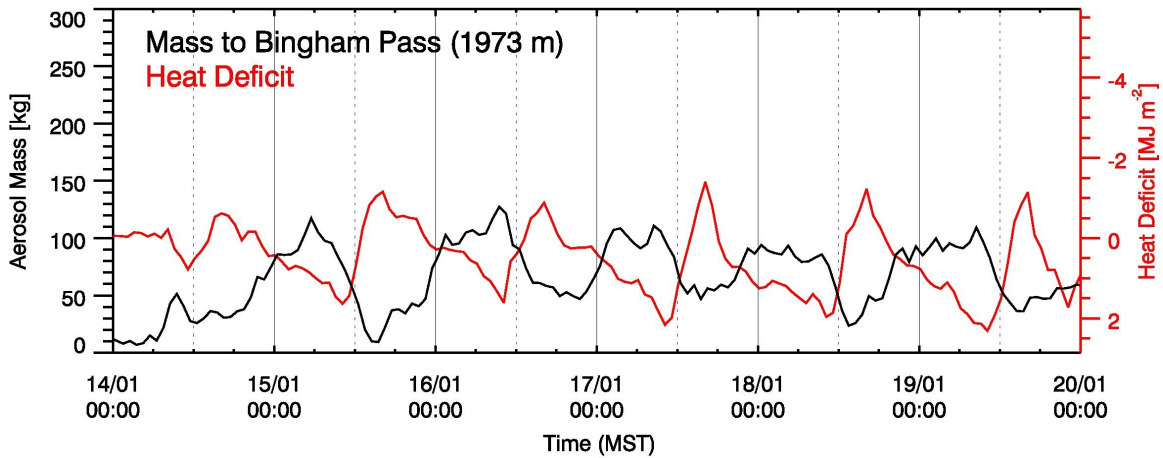

Figure 29. Volume weighted equivalent $PM_{2.5}$ aerosol mass to Bingham Pass (blue) and the heat deficit between 1500 and 1950 m MSL (red) for the period from 14 to 20 January 2014.

7. Application of the mathematical model to a representative composite day

7.1 Emission and storage rates in the control volume

In this section we composite hourly data from 1200 MST 15 January 2014 to 1800 MST 19 January 2014 (see the shaded area in Figure 28) to obtain hourly data for a mean day. This compositing period was chosen because the series of days exhibited very similar features in the temporal and spatial distribution of equivalent particulate concentrations and the mean day thus

34

represents a typical dry, quiescent, non-cloudy cold-air pool day. This day will be used to illustrate the computation of ventilation and release fractions.

From the emissions data in section 6a we calculated hourly emission rates for $PM_{2.5}$ and PM_{10} for the composite day. The daily particulate emissions for the composite day were 451 and 4012 kg/day, so that the hourly values became 18.78 and 167.15 kg/hour for $PM_{2.5}$ and PM_{10}, respectively.

The variation of hourly storage rates were determined for the composite day in a similar manner, with the variation of equivalent particulate mass stored in the control volume atmosphere shown in Figure 30. Also shown on the figure is the mean rate of change of equivalent particulate mass between the afternoon minimum and the morning maximum for $PM_{2.5}$ and PM_{10}.
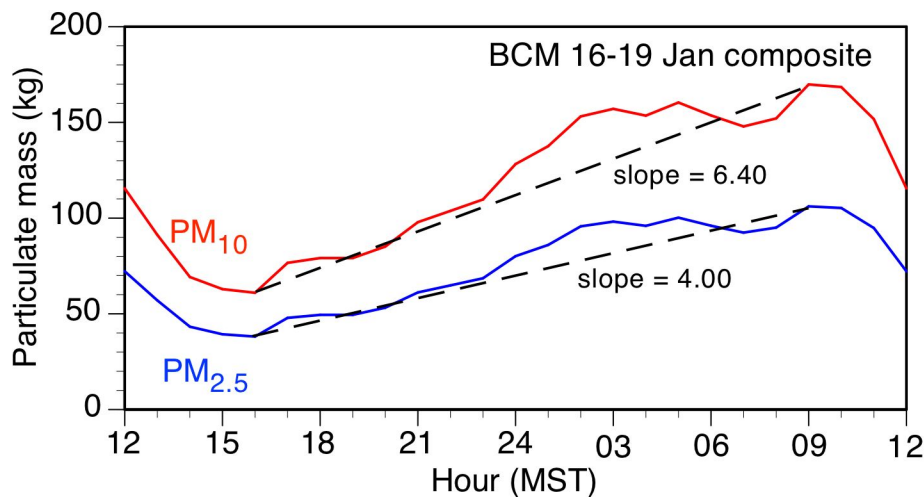

Figure 30. Volume-weighted equivalent $PM_{2.5}$ and PM_{10} mass (to Bingham Pass) stored in the control volume atmosphere versus time of day for the composite mean day. The mean rate of change of equivalent particulate mass for this composite day between the 1600 minimum and the 0900 MST maximum (when no ventilation occurs) is 4.00 kg h^{-1} for $PM_{2.5}$ and 6.40 kg h^{-1} for PM_{10}.

7.2. Deposition rates within the control volume

Surprisingly little is known in general about dry deposition rates, which have been reported by previous investigators to vary over orders of magnitude (Ruijgrok et al. 1995). The dry deposition process that is most applicable to particulate deposition in the mine during non-cloudy and non-precipitating periods is gravitational settling. Examples of the different settling rates for particles of different size were given in Table 1. During the nighttime storage buildup period (1600 to 0900 MST), particulates are assumed trapped in the mine (V = 0) and the deposition rate is the difference between the emission and storage rates, D = E - S. During the daytime storage breakdown period (0900 to 1600 MST), deposition is assumed to continue at the mean nighttime rate.

7.3. Ventilation rates of the mine control volume

Ventilation is negligible during nighttime (V=0). During daytime, ventilation is given by the effective emission rate (E - D) plus the decrease in storage rate so that V = (E - D) - S.

8. Results for the composite day

Hourly mass tendency budgets for $PM_{2.5}$ and PM_{10} for the composite day are shown in Figure 31 a and b. Because our method calculates both equivalent $PM_{2.5}$ and PM_{10} concentrations as linear functions of the same backscatter values the shapes of the rate curves are exactly the same, while the rate values differ for the two size classes of particulates. Considering first the results for PM_{10}, the emission and deposition rates are much larger than the ventilation and storage rates. Thus, on typical cold-air pool days dry deposition in the mine removes most of the mine emissions because of the long night and the appreciable settling velocity of PM_{10} particulates in the quiescent mine atmosphere. On the other hand, the $PM_{2.5}$ emission and deposition rates are not so large relative to the ventilation and storage rates. In the case of PM_{10}, the particulate ventilation from the mine is a small fraction of the emissions, and a large fraction of the aerosols that accumulate in the mine atmosphere (storage) are ventilated from the mine daily. For $PM_{2.5}$, the particulate ventilation rate from the mine is a relatively large fraction of the emissions rate and even exceeds the emission rate during mid-day. The relative value of the terms can be best evaluated by time integrations and daily ratios among the terms.
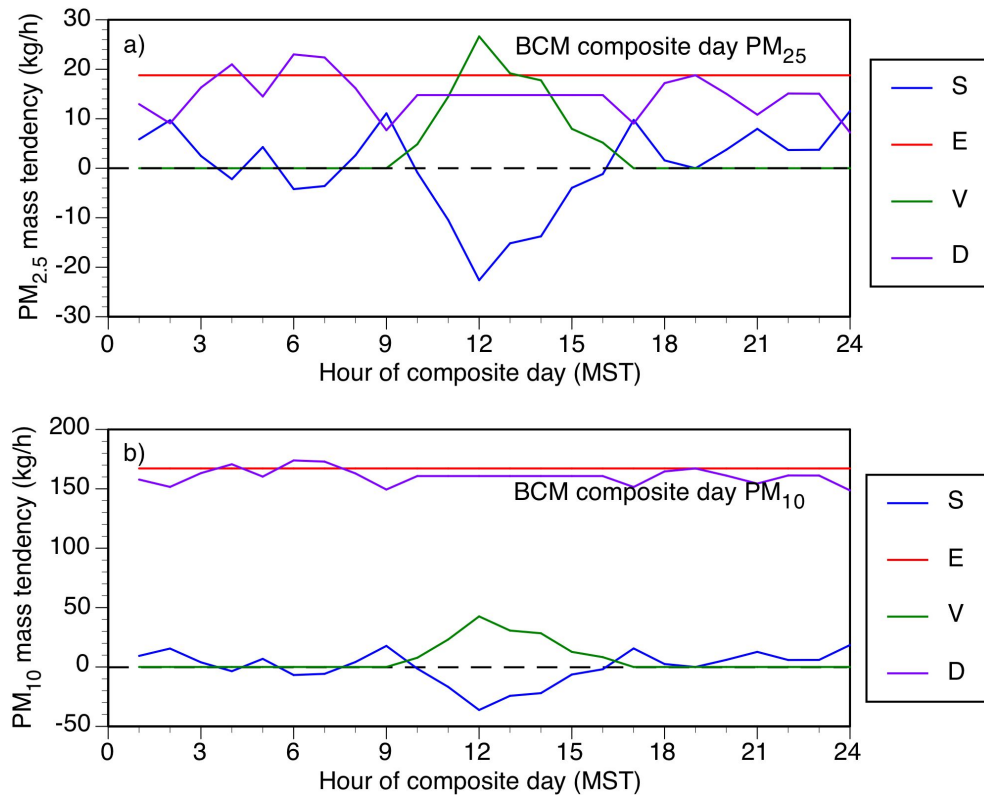

Figure 31. Mass tendencies (rates) for a) $PM_{2.5}$ and b) PM_{10} for the composite day.

Because the 24-hour composite day begins and ends with the same rate values, a daily integration (Table 2) gives a net result of 0 for the storage term. On the other hand, the emission, ventilation and deposition terms accumulate during the day. Emissions add to 451 and 4012 kg for $PM_{2.5}$ and PM_{10}, with somewhat lower values for daily total deposition. The ventilation term removes about 96 and 154 kg of $PM_{2.5}$ and PM_{10} particulates from the mine on a daily basis.

Table 2. Daily total masses for the composite day.

Term	$PM_{2.5}$ (kg)	PM_{10} (kg)
S	0	0
E	451	4012
V	96	154
D	355	3858

Ratios of the individual daily terms are shown in Table 3. Nearly 79% of the $PM_{2.5}$ emissions are deposited within the mine during a typical cold-air pool day, as the particles settle slowly through the course of the long night. Of the amount remaining in the mine atmosphere, however, 72% is ventilated, resulting in an escape fraction of 21%. A much larger fraction, 96%, of the PM_{10} aerosol mass emitted within the enclosed mine volume is deposited within the mine on a typical dry, non-cloudy cold-air pool day in mid-winter. Only about 4% of the emissions lead to an increase in the atmospheric burden or escape from the mine. Of the PM_{10} aerosols that accumulate in the mine atmosphere overnight, 72% are ventilated during daytime. None of these ratios or mass calculations account for chemical reactions that produce secondary particulates. Dust produced by mining activities will settle on the mine surfaces, and the daily PM_{10} dust depth increment d can be calculated using the formula $d = 1/\rho\ D/A = 0.23$ μm/day or 0.08 mm/year, where the daily deposition D is 3858 kg, the rock density ρ is 2800 kg m^{-3} and the projected horizontal area A of the control volume (Figure 4) is about 6 km^2 or 6 x 10^6 m^2.

Table 3. Selected daily ratios. Here, D, E and V represent daily totals rather than hourly rates.

Daily fractions	$PM_{2.5}$	PM_{10}
Escape fraction (V/E)	0.213	0.038
Ventilation fraction A (S_{max}-S_{min})/S_{max}	0.641	0.641
Ventilation fraction B (*)	0.716	0.716
Deposition fraction (D/E)	0.787	0.962

*ventilation fraction B accounts for the fact that the effective emissions that occur during the time of ventilation are also being evacuated from the volume as well as the storage change. The formula for the ventilation fraction B is (S_{max} + (E - D) * Δt - S_{min})/(S_{max} + (E - D) * Δt), where D is at the mean nighttime deposition rate and Δt is the 7-h time period over which ventilation occurs.

Looking back at Figure 30, the rate of increase of mass storage in the mine atmosphere slows around 0200 MST. This change in rate is not yet fully understood. From (5), assuming that the emission rate of primary particulate emissions is constant, this suggests 1) a decrease in the chemical conversion of gaseous precursors to secondary particulates, 2) an increase in dry

deposition or 3) an increase in particulate ventilation from the BCM. This change in rate is presently an unknown that could affect the results. There are ways to investigate this further using data that are in-hand, as will be specified below in section 11.

9. Advantages and disadvantages of the new method

In this section, we would like to enumerate the advantages and disadvantages of this new method for determining aerosol escape from the BCM. The new method has a key advantage over the previous Computational Fluid Dynamics model simulations (Bhaskar and Tandon 1996). The CFD simulations are incapable of simulating the meteorological mechanisms leading to particulate escape from the mine in cold-air pool conditions -- it cannot accurately simulate a full diurnal cycle in which stability and winds vary in space and time, a common situation in complex terrain meteorology where boundary layers form along slopes and insolation differs on the sidewalls. On the other hand, the new method has the disadvantage that it has never been used before and is thus not a familiar or validated approach and is focused on only the enclosed part of the mine, without considering emissions outside or above the control volume. The new method is based on observations rather than a model and thus is somewhat more intuitive to those unfamiliar with modeling approaches. The new method requires that a backscatter-concentration relationship be developed for the mine in order to estimate the escape fraction. This will require new observations including measurement of aerosol concentrations in the mine. Because the aerosol characteristics are not expected to change greatly during the ventilation period, ventilation fractions as calculated with the new method are expected to be robust and reasonably accurate. Further, no knowledge of particulate emission rates in the mine is required to compute ventilation fractions, an advantage over computing a release fraction, particularly since the rate of secondary particulate formation in the mine is a major unknown. Further, the ventilation fraction depends only on the relative change in aerosol mass rather than its absolute value. Thus the ventilation fraction is independent of the slope of the linear $PM_{2.5}$-backscatter relationship. For instance, if the true slope of the regression line in Figure 22 were only 50% of the presently calculated value, the computed ventilation fraction would be unchanged. The new approach would need further development to apply to non cold-air pool events in which, for example, non-diurnal particulate escapes occurred. Despite the advantages of using ventilation fractions rather than escape fractions, some regulatory models require an escape fraction and are not designed to use ventilation fractions.

10. Conclusions

Analysis of meteorological data from the Bingham Canyon Mine and the adjacent Salt Lake Valley during persistent, multi-day, mid-winter cold-air pools or inversions has investigated the meteorological mechanisms that lead to aerosol escape from the Bingham Mine. The aerosol escape occurs on a daily basis and is caused by insolation that illuminates the south-facing sidewall of the mine during daytime. An upslope flow occurs in the heated layer of air above the slope. To replace this evacuated air a cross-basin flow occurs bringing aerosol-laden air to the sidewall where it is fumigated into the heated convective boundary layer and carried upslope. Compensatory sinking of cleaner air from aloft occurs over the remainder of the mine atmosphere. This process is very regular under the typical large-scale atmospheric conditions

associated with multi-day inversions (dry, clear conditions with weak winds aloft and with a high pressure ridge over the Pacific coast or Intermountain Basin). The meteorological mechanisms associated with this pollutant mass removal from the mine are supported by observations made inside the mine with a vertically pointing aerosol lidar from which changes in aerosol loading in the mine can be seen, as well as sinking of cleaner air into the mine during the daytime aerosol removal period.

The diurnal changes of aerosol burden in the mine suggest that a new method relying on observations from an aerosol lidar can be developed to monitor the ventilation of aerosols from the mine. We have developed such a method and documented it fully in this report, including the mathematical equations that provide the basis for the new method. To use this method with confidence, an aerosol backscatter-concentration relationship must be developed for the specific mix of aerosols in the mine. Because the particulate concentration data necessary to develop this relationship were unavailable in the mine, we have illustrated the application of the new method for the mine by using a relationship developed in the adjacent Salt Lake Valley with an identical aerosol lidar. Thus, since a major assumption is required (that the aerosol characteristics affecting lidar backscatter are the same in the BCM and SLV), results for the mine should not be considered definitive, but only illustrative of the method. We therefore refer to the concentration and mass estimates calculated under this assumption as *equivalent* concentration and *equivalent* aerosol mass. A second key assumption, that aerosols are horizontally homogeneous within the mine while varying with height, is thought to be a reasonable assumption if applied to the portion of the mine that is fully enclosed by topography.

The method has thus been applied to the mine *under the assumptions stated*, finding that a large fraction of the aerosols that have accumulated in the mine atmosphere in mid-morning are ventilated from the mine during the day by the meteorological mechanisms previously mentioned. Only a small part of the nighttime emissions of PM_{10}, however, are suspended in the atmosphere during the ventilation period due to high deposition rates. Thus, even if the effective emissions during the ventilation period are also ventilated, the aerosol escape fraction of PM_{10} is well within the escape fraction estimates of Bhaskar and Tandon (1996). It is worth noting that the ventilation fraction, which has only a weak dependence on concentrations or aerosol burden from the backscatter-concentration relationship, is a more robust and accurate measurement of aerosol escape from the mine. This variable, which does not require an estimate of the uncertain mine emissions, might be a better way of estimating aerosol escape from the mine than the escape fraction.

The application of the new method to $PM_{2.5}$ has illuminated some issues that are not entirely obvious. Because the settling velocity of these aerosols is small, they tend to be retained in the mine atmosphere longer than the larger aerosols. Thus, by morning there is a higher fraction of them suspended in the mine atmosphere that will be ventilated by the meteorological mechanisms previously described. Following this new approach, the ventilation fraction will be the same as for PM_{10} aerosols. The deposition rate of $PM_{2.5}$ is lower than for the larger particles and the escape fraction is higher.

While the aerosol calculations have focused on aerosol escape from the mine, it is important to keep in mind a key finding from the meteorological investigations that are relevant to the high $PM_{2.5}$ exceedances that occur in the adjacent Salt Lake Valley during cold-air pool events. Particulates escaping from the mine, because they are carried in air that is potentially warmer than the air at the floor of the Salt Lake Valley below the mine during wintertime inversions, are unlikely to be transported to the valley floor and are thus not expected to contribute significantly to $PM_{2.5}$ concentrations at the valley floor during multi-day SLV inversion events.

11. Recommendations for future work

The scientific basis for the escape fraction estimates could be strengthened with additional analyses of project data and through additional research and field observations.

• We recommend that field experiments be conducted in the BCM to gain the information necessary to support escape fraction estimates, regardless of which method or models are chosen for improving current estimates. The experiments should, as a minimum, measure $PM_{2.5}$ and PM_{10} concentrations inside the mine, as these will be crucial for validating any method of estimating escape fractions. We have put considerable thought into the timing, equipment and personnel requirements for a field study, but would need guidance regarding the study goals, which might extend beyond the multi-day wintertime cold-air pools that we have studied to date. Such studies would need to be designed to fit safely into the activities within the operational mine. Minimum data to support the aerosol lidar method would require contemporaneous hourly measurements of backscatter and $PM_{2.5}$ and PM_{10} concentrations, relative humidity, and information on secondary formation of particulates.

• A number of additional analyses will strengthen our findings. First, analyses accomplished for the composite day should be extended to individual days of the 15-day cold-air pool period. More thought should also be expended on determining ways to establish error bars. Additional analyses of existing meteorological data may help to determine the causes of the significant variation in BCM aerosol ventilation fraction from day to day and the causes of the sudden nighttime decrease in aerosol storage at ~0200 MST on many days of the cold-pool episode. This decrease is not accounted for in our calculations and might be caused by ventilation of aerosols from the mine related to mixing from downslope cold-air inflows. A better estimate of aerosol deposition could be obtained if we could find a day when the ceilometer was operational, emissions were known and the ceilometer verified that there was no aerosol escape from the enclosed portion of the mine.

• Our scanning Doppler wind lidar was operated in the BCM during different winters (2010-2011 and 2011-2012) than the ceilometer (2012-2013 and 2013-2014). A full analysis of the range-height indicator (RHI), vertical stare and velocity-azimuth display (VAD) data may strengthen conclusions about the meteorological mechanisms leading to aerosol ventilation. For example, the vertical stares may have sufficient resolution to see the sinking of air over the mine center that compensates for upward motions in the upslope layer on the south-facing sidewall. The lidar was operated during some windy periods and the lidar wind and backscatter information during these events may provide information on aerosol ventilation

during windy periods. RHI scans were made across the pit; these may provide information on the upslope flow layer and any horizontal axis rotating eddies that form in the upper altitudes of the mine. Future experiments could include lidar scanning strategies aimed at gaining detail on the upslope flows on the insolated sidewall.

• Additional information on the cross-basin flow in the mine could come from an analysis of stagnation, ventilation and recirculation at different lidar range gates using an approach developed by Allwine and Whiteman (1994).

• A more comprehensive study of the meteorological mechanisms leading to the wintertime ventilation of the mine during cold-air pool periods could be obtained from modern full-physics numerical model simulations. We have recently used the WRF and CM1 models to simulate insolation differences and subsequent cross basin and upslope flows in Arizona's Meteor Crater basin and are presently conducting a similar project under NSF funds for a limestone sinkhole basin in the Eastern Alps. We are also using MESO12 to study hydraulic flows into the Meteor Crater basin. These models can handle the meteorology and physics in complex terrain much more effectively than earlier models. Nonetheless, none of these models have yet been tested in basins as deep and steep-walled as the Bingham Canyon Mine.

• Additional meteorological analyses could be focused on comparing meteorological and aerosol distribution and loading relationships in the BCM and SLV. Initial analyses have found that aerosol concentrations are lower in the SLV, but that the timing of diurnal oscillations is out of phase with BCM.

REFERENCES:

Adler, B., C. D. Whiteman, S. W. Hoch, M. Lehner, and N. Kalthoff, 2012: Warm air intrusions in Arizona's Meteor Crater. *J. Appl. Meteor. Climatol.*, **51**, 1010-1025.

Allwine, K. J., and C. D. Whiteman, 1983: Operational Guide to MELSAR-A Mesoscale Complex Terrain Air Quality Model. PNL-4732, Pacific Northwest Laboratory, Richland, Washington, 44 pp.

Allwine, K. J., and C. D. Whiteman, 1984: Technical Description of MELSAR: A Mesoscale Air Quality Model for Complex Terrain. PNL-5048, Pacific Northwest Laboratory, Richland, Washington, 97 pp.

Allwine, K. J., and C. D. Whiteman, 1985: MELSAR: A Mesoscale Air Quality Model for Complex Terrain. Volume 1 - Overview, Technical Description and User's Guide and Volume 2 - Appendices. PNL-5460, Pacific Northwest Laboratory, Richland, Washington, 155 and 358 pp.

Allwine, K. J., and C. D. Whiteman, 1988: Ventilation of pollutants trapped in valleys: A simple parameterization for regional-scale dispersion models. *Atmos. Environ.*, **22**, 1839-1845.

Allwine, K. J., and C. D. Whiteman, 1994: Single-station integral measures of atmospheric stagnation, recirculation and ventilation. *Atmos. Environ.* , **28**, 713-721.

Allwine, K. J., X. Bian, C. D. Whiteman, and H. W. Thistle, 1997: VALDRIFT–A valley atmospheric dispersion model. *J. Appl. Meteor.*, **36**, 1076-1087.

Bader, D. C., and T. B. McKee, 1983: Dynamical model simulation of the morning boundary layer development in deep mountain valleys. *J. Climate Appl. Meteor.*, **22**, 341-351.

Bader, D. C., and T. B. McKee, 1985: Effects of shear, stability and valley characteristics on the destruction of temperature inversions. *J. Climate Appl. Meteor.*, **24**, 822-832.

Bader, D. C., and C. D. Whiteman, 1989: Numerical simulation of cross-valley plume dispersion during the morning transition period. *J. Appl. Meteor.*, **28**, 652-664.

CH2MHILL, 2011: Final Report, Bingham Canyon Mine Expansion Technical Support Document. Revision of January 2011 as submitted to UDAQ by KUC LLC.

Dorninger, M., C. D. Whiteman, B. Bica, S. Eisenbach, B. Pospichal, and R. Steinacker, 2011: Meteorological events affecting cold-air pools in a small basin. *J. Appl. Meteor. Climatol.*, **50**, 2223-2234.

Emeis, S., 2011: *Surface-based Remote Sensing of the Atmospheric Boundary Layer*. Atmospheric and Oceanographic Sciences Library, **40**, 174pp.

Gan, C. M., Y-H Wu, B. Gross, and F. Moshary, 2010: Statistical comparison between HYSPLIT sounding and lidar observation of planetary boundary layer characteristics over New York City. Laser Radar Technology and Applications XV, edited by M. D. Turner and G. W. Kamerman. *Proc. of SPIE*, **7684**, 76841K-1 through 76841K-10. doi:10.1117/12.849705.

Hoch, S. W., and C. D. Whiteman, 2010: Topographic effects on the surface radiation balance in and around Arizona's Meteor Crater. *J. Appl. Meteor. Climatol.*, **49**, 1114-1128.

Hoch, S. W., C. D. Whiteman, and B. Mayer, 2011: A systematic study of longwave radiative heating and cooling within valleys and basins using a three-dimensional radiative transfer model. *J. Appl. Meteor. Climatol.*, **50**, 2473-2489.

Lapple, C. E., 1961: Characteristics of particles and particle dispersoids. Stanford Research Institute Journal.

Lehner, M., and C. D. Whiteman, 2014: Physical mechanisms of the thermally driven cross-basin circulation. *Quart. J. Roy. Meteor. Soc.*, **140**, 895-907.

Lehner, M., and C. D. Whiteman, 2012: The thermally driven cross-basin circulation in idealized basins under varying wind conditions. *J. Appl. Meteor. Climatol.*, **51**, 1026-1045.

Lehner, M., C. D. Whiteman, and S. W. Hoch, 2011: Diurnal cycle of thermally driven cross-basin winds in Arizona's Meteor Crater. *J. Appl. Meteor. Climatol.*, **50**, 729-744.

Markowski, P., and Y. Richardson, 2010: *Mesoscale Meteorology in Midlatitudes*. John Wiley and Sons, Ltd., West Sussex, UK, 407pp.

Melfi, S. H., J. D. Spinhirne, S. H. Chou, and S. P. Palm, 1985: Lidar observation of the vertically organized convection in the planetary boundary layer over the ocean. *J. Clim. Appl. Meteor.*, **24**, 806-821.

Müller, H., and C. D. Whiteman, 1988: Breakup of a nocturnal temperature inversion in the Dischma Valley during DISKUS. *J. Appl. Meteor.*, **27**, 188-194.

Münkel, C., N. Eresmaa, J. Räsänen, and A. Karppinen, 2007: Retrieval of mixing height and dust concentration with lidar ceilometer. *Bound.-Layer Meteor.*, **124**, 117-128. doi:10.1007/s10546-006-9103-3.

Münkel, C., S. Emeis, W. J. Müller, and K. Schäfer, 2003: Observation of aerosol in the mixing layer by a ground-based lidar ceilometer. Remote Sensing of Clouds and the Atmosphere VII, K. Schäfer, O. Lado-Bordowsky, A. Comerón, and R. H. Picard, Eds. *Proc. of SPIE*, **4882**, 344-352.

Münkel, C., S. Emeis, W. J. Müller, and K. Schäfer, 2004: Aerosol concentration measurements with a lidar ceilometer: results of a one year measuring campaign. Remote Sensing of Clouds

and the Atmosphere VIII, K. P. Schäfer, A. Comerón, M. R. Carleer, and R. H. Picard, Eds. *Proc. of SPIE*, **5235**, 486-496. doi:10.1117/12.511104.

Pankow, K. L., J. R. Moore, J. M. Hale, K. D. Koper, T. Kubacki, K. M. Whidden, and M. K. McCarter, 2013: Msssive landslide at Utah copper mine generates wealth of geophysical data. *GSA Today*, **24**, 4-9. https://rock.geosociety.org/gsatoday/archive/24/1/pdf/i1052-5173-24-1-4.pdf

Rendón, A. M., 2014: Interplay between the temperature inversion and urban heat island in idealized urban valleys with impacts on air quality. Ph.D. dissertation. University of Antioquia, Medellín, Colombia, 75pp.

Ruijgrok, W., C. I. Davidson, and K. W. Nicholson, 1995: Dry deposition of particles. *Tellus*, **47B**, 587-601.

Silcox, G. D., K. E. Kelly, E. T. Crosman, C. D. Whiteman, and B. L. Allen, 2012: Wintertime PM2.5 concentrations in Utah's Salt Lake Valley during persistent, multi-day cold-air pools. *Atmos. Environ.*, **42**, 17-24.

Stull, R. B., 1988: *An Introduction to Boundary Layer Meteorology*. Kluwer Academic PublishersDordrecht, Netherlands. 666pp.

Sundström, A.-M., T. Nousiainen, and T. Petäjä, 2009: On the quantitative low-level aerosol measurements using ceilometer-type lidar. *J. Atmos. Oceanic Technol.*, **26**, 2340-2352.

United States Environmental Protection Agency (EPA), 1985, as updated through 2008. AP-42, Fifth Edition: Compilation of Air Pollutant Emission Factors, Volume 1: Stationary point and Area Sources. Available at http://www.epa.gov/ttn/chief/ap42/#drafts.

United States Environmental Protection Agency (EPA), 2004a: Exhaust and Crankcase Emission Factors for Nonroad Engine Modeling – Compression-Ignition. Assessment and Standards Division, Office of Transportation and Air Quality. EPA420-P-04-009, NR-009c. April.

United States Environmental Protection Agency (EPA), 2004b: Median Life, Annual Activity, and Load Factor Values for Nonroad Engines Emissions Modeling. Assessment and Standards Division, Office of Transportation and Air Quality. EPA420-P-04-005, NR-005c. April.

Vaisala, 2012: User's Guide, Vaisala Ceilometer CL31. Vaisala Oyj, Helsinki, Finland, 136pp.

Whiteman, C. D., 1982: Breakup of temperature inversions in deep mountain valleys: Part I. Observations. *J. Appl. Meteor.*, **21**, 270-289.

Whiteman, C. D., 1989: Morning transition tracer experiments in a deep narrow valley. *J. Appl. Meteor.*, **28**, 626-635.

Whiteman, C. D., 1990: Observations of Thermally Developed Wind Systems in Mountainous Terrain. Chapter 2 in Atmospheric Processes Over Complex Terrain, (W. Blumen, Ed.), *Meteorological Monographs*, **23**, no. 45. American Meteorological Society, Boston, Massachusetts, 5-42.

Whiteman, C. D., 2000: *Mountain Meteorology: Fundamentals and Applications*. Oxford University Press, New York, 355pp.

Whiteman, C. D., and K. J. Allwine, 1985: VALMET - A Valley Air Pollution Model. Final Report. PNL-4728, Rev. 1. Pacific Northwest Laboratory, Richland, Washington, 176 pp.

Whiteman, C. D., and S. W. Hoch, 2014: Pseudo-vertical temperature profiles in a broad valley from lines of temperature sensors on the sidewalls. *J. Appl. Meteor. Climatol.*, **53**, 2430-2437.

Whiteman, C. D., and T. B. McKee, 1978: Air pollution implications of inversion descent in mountain valleys. *Atmos. Environ.*, **12**, 2151-2158.

Whiteman, C. D., and T. B. McKee, 1982: Breakup of temperature inversions in deep mountain valleys: Part II. Thermodynamic model. *J. Appl. Meteor.*, **21**, 290-302.

Whiteman, C. D., S. W. Hoch, and M. Lehner, 2010: Nocturnal cold air intrusions into a closed basin: Observational evidence and conceptual model. *J. Appl. Metor. Climatol.*, **49**, 1894-1905.

Whiteman, C. D., J. M. Hubbe, and W. J. Shaw, 2000: Evaluation of an inexpensive temperature data logger for meteorological applications. *J. Atmos. Oceanic Technol.*, **17**, 77-81.

Whiteman, C. D., S. W. Hoch, J. D. Horel, and A. Charland, 2014: Relationship between particulate air pollution and meteorological variables in Utah's Salt Lake Valley. *Atmos. Environ.*, **94**, 742-753.

Whiteman, C. D., B. Pospichal, S. Eisenbach P. Weihs, C. B. Clements, R. Steinacker, E. Mursch-Radlgruber, and M. Dorninger, 2004: Inversion breakup in small Rocky Mountain and Alpine basins. *J. Appl. Meteor.*, **43** (8), 1069-1082.

Whiteman, C. D., S. Zhong, and X. Bian, 1999: Wintertime boundary-layer structure in the Grand Canyon. *J. Appl. Meteor.*, **38**, 1084-1102.

Young, J. S., and C. D. Whiteman, 2014: Laser ceilometer investigation of persistent wintertime cold-air pools in Utah's Salt Lake Valley. *J. Appl. Meteor. Climatol.* Submitted.

Zardi, D., and C. D. Whiteman, 2012: Diurnal Mountain Wind Systems. Chapter 2 in: *Mountain Weather Research and Forecasting* (Chow, F. K., S. F. J. DeWekker, and B. Snyder (Eds.)). Springer, Berlin, pp 35-119.
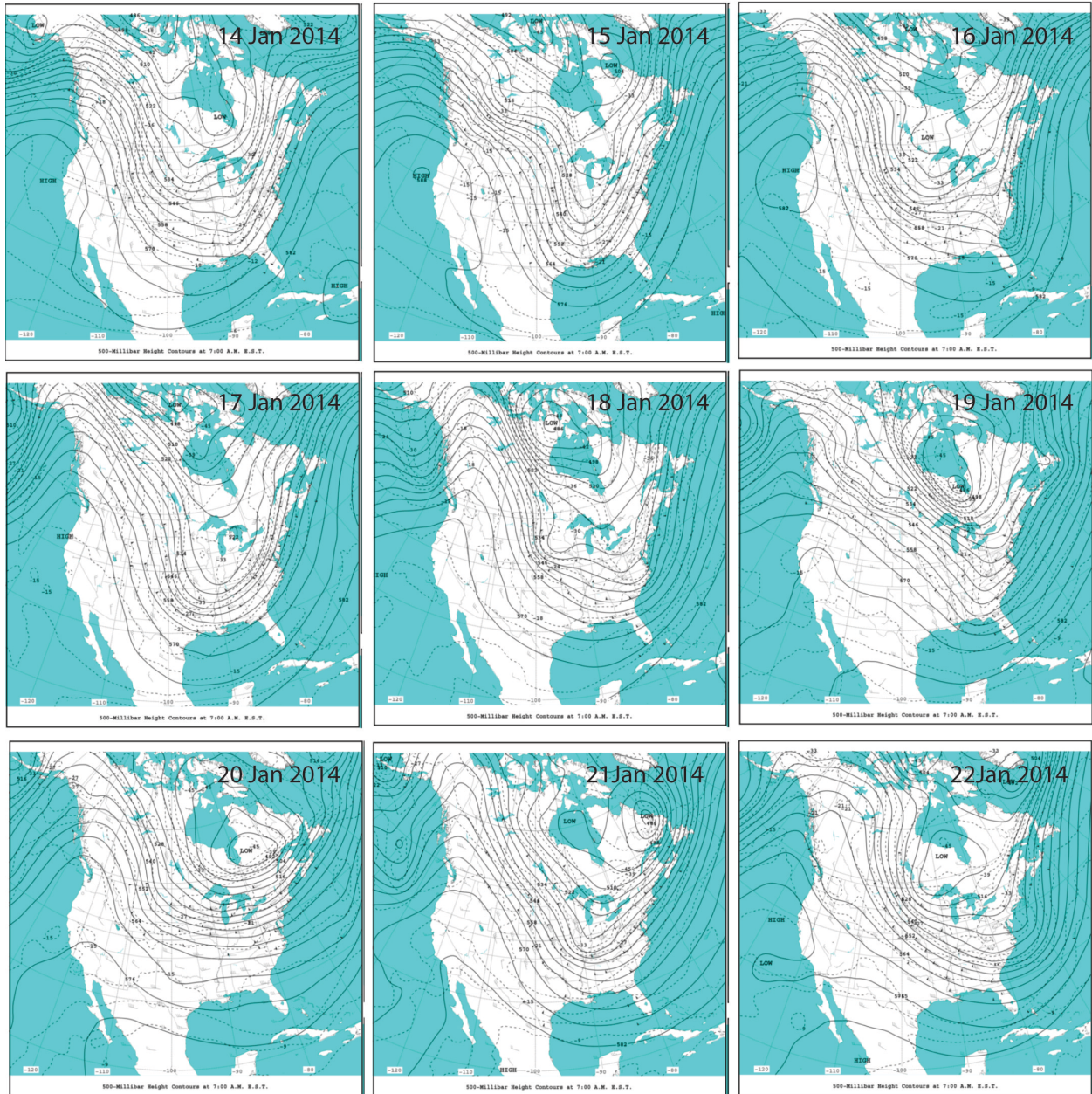
APPENDIX A - 500 mb charts

Figure A1. 500 mb weather charts for 14-22 January 2014. The maps are for 0500 MST (0700 EST). From NOAA's Daily Weather Maps, Weekly Series.
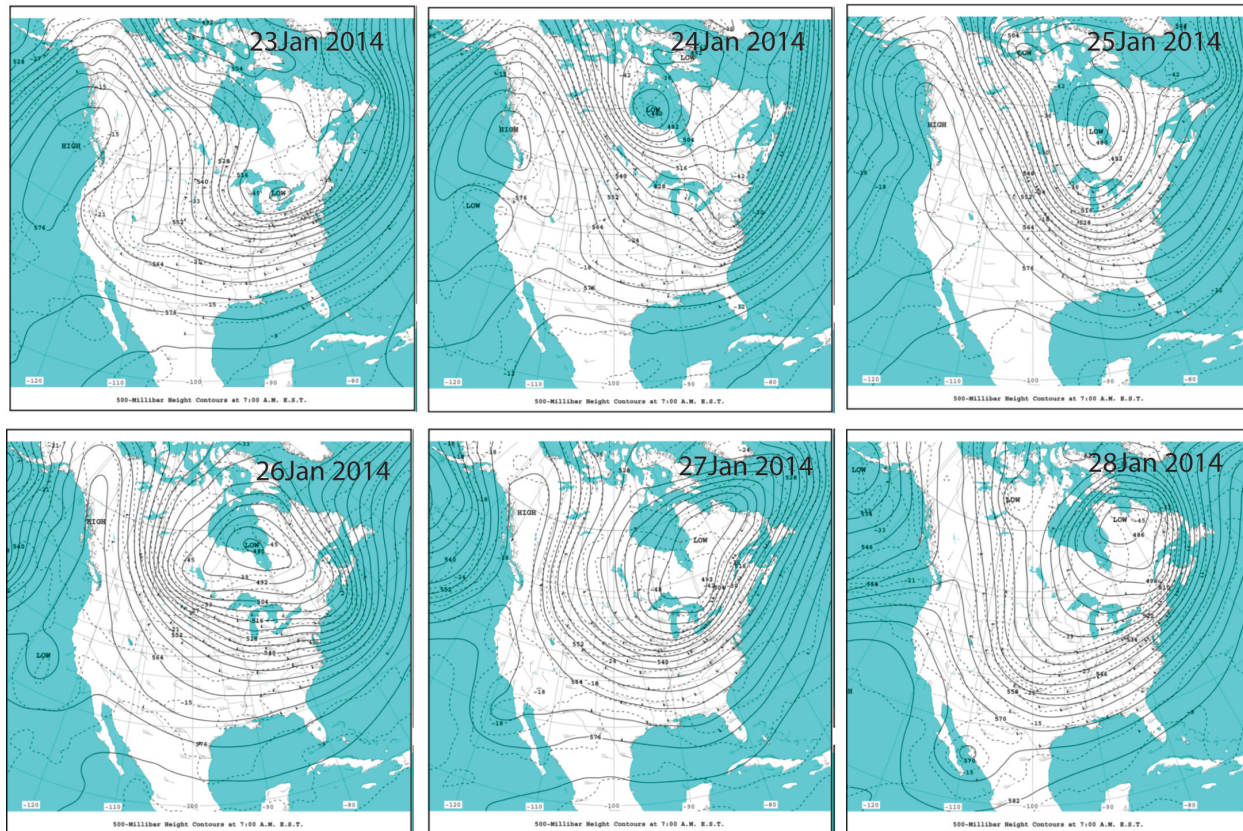
Figure A2. 500 mb weather charts for 23-28 January 2014. The maps are for 0500 MST (0700 EST). From NOAA's Daily Weather Maps, Weekly Series.
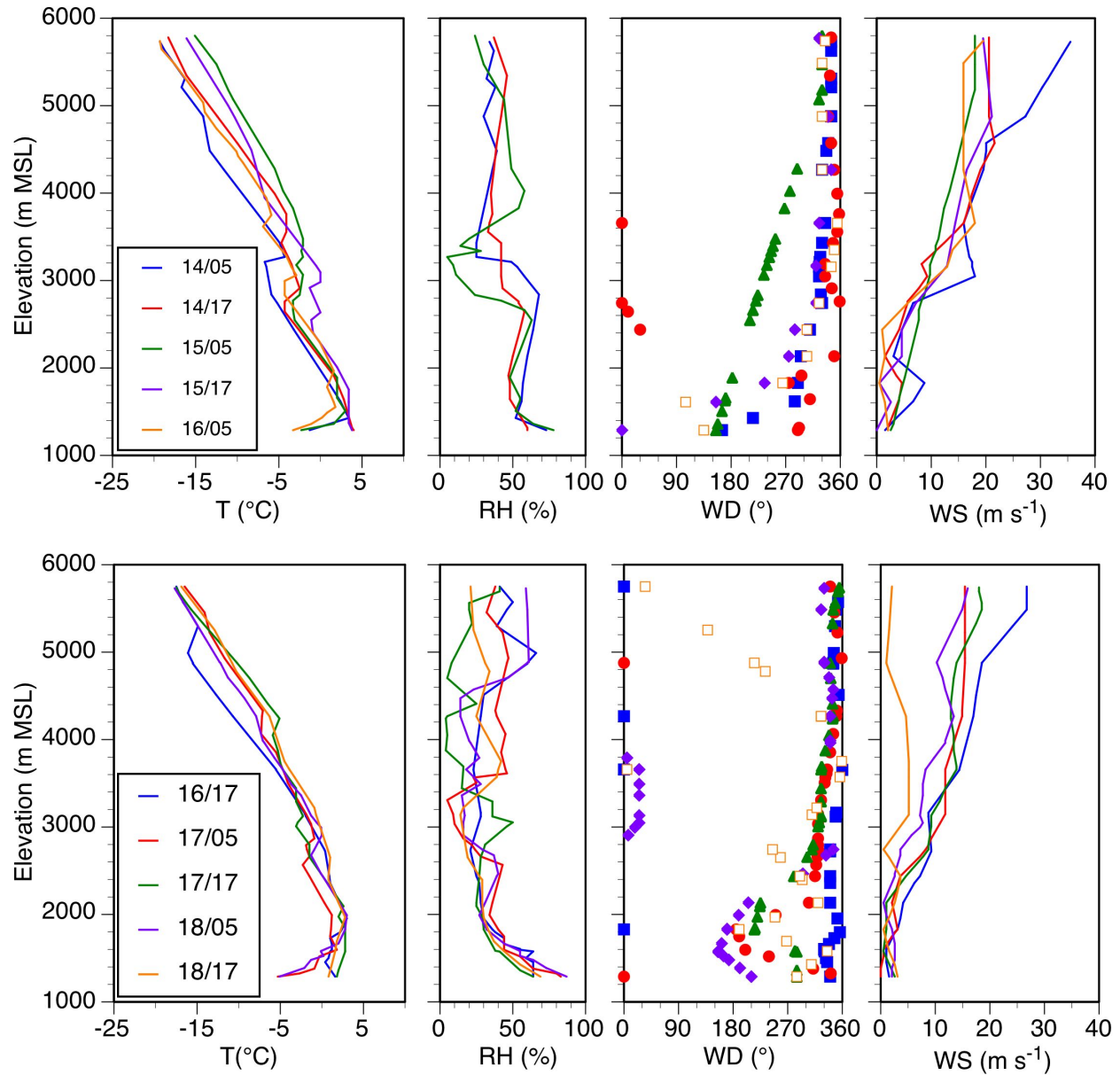
APPENDIX B - Radiosonde data

Figure B1. Salt Lake City radiosonde soundings from 0500 MST 14 January to 1700 MST 18 January 2014. Shown are soundings of temperature, relative humidity, wind direction and wind speed.
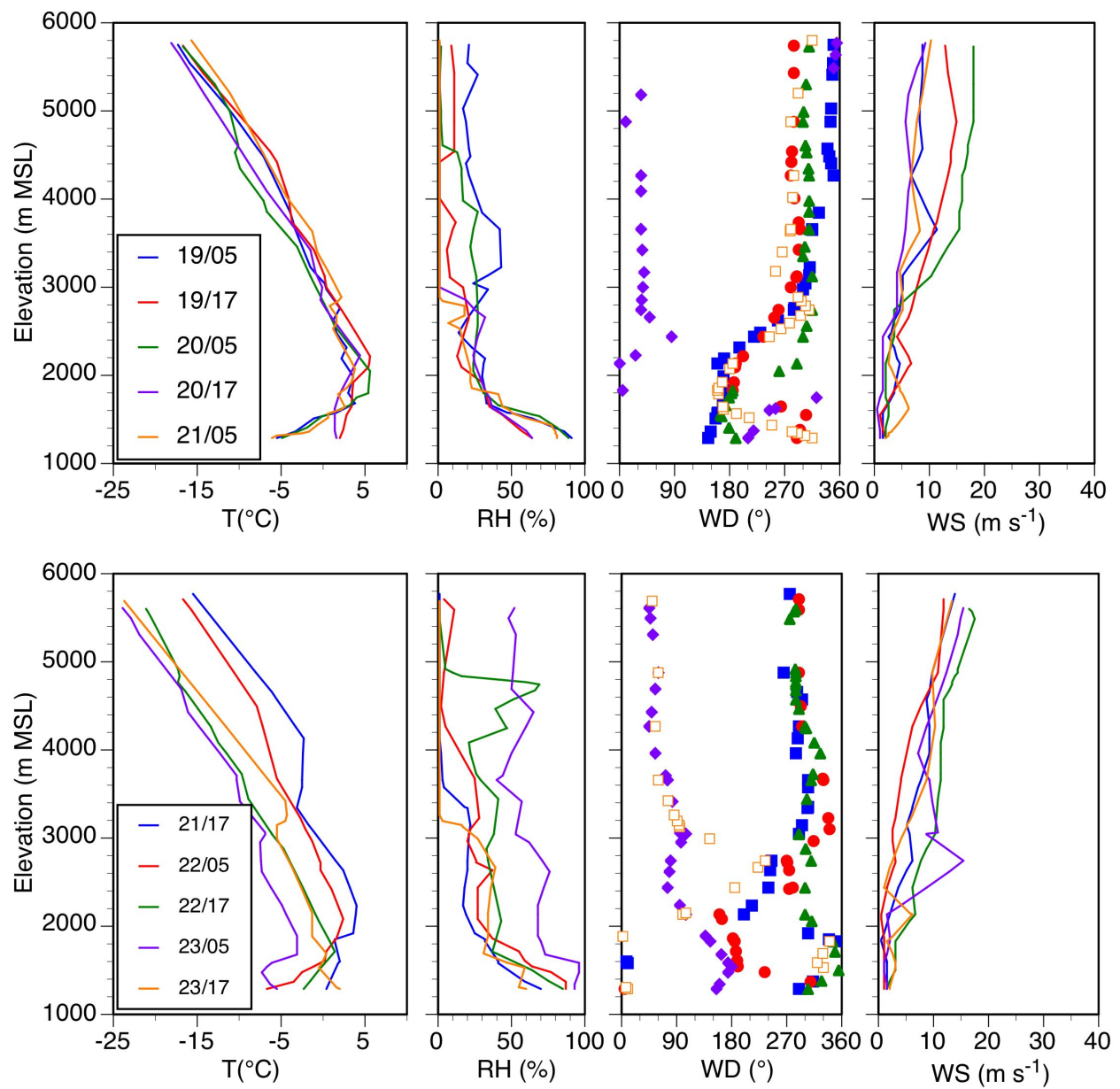
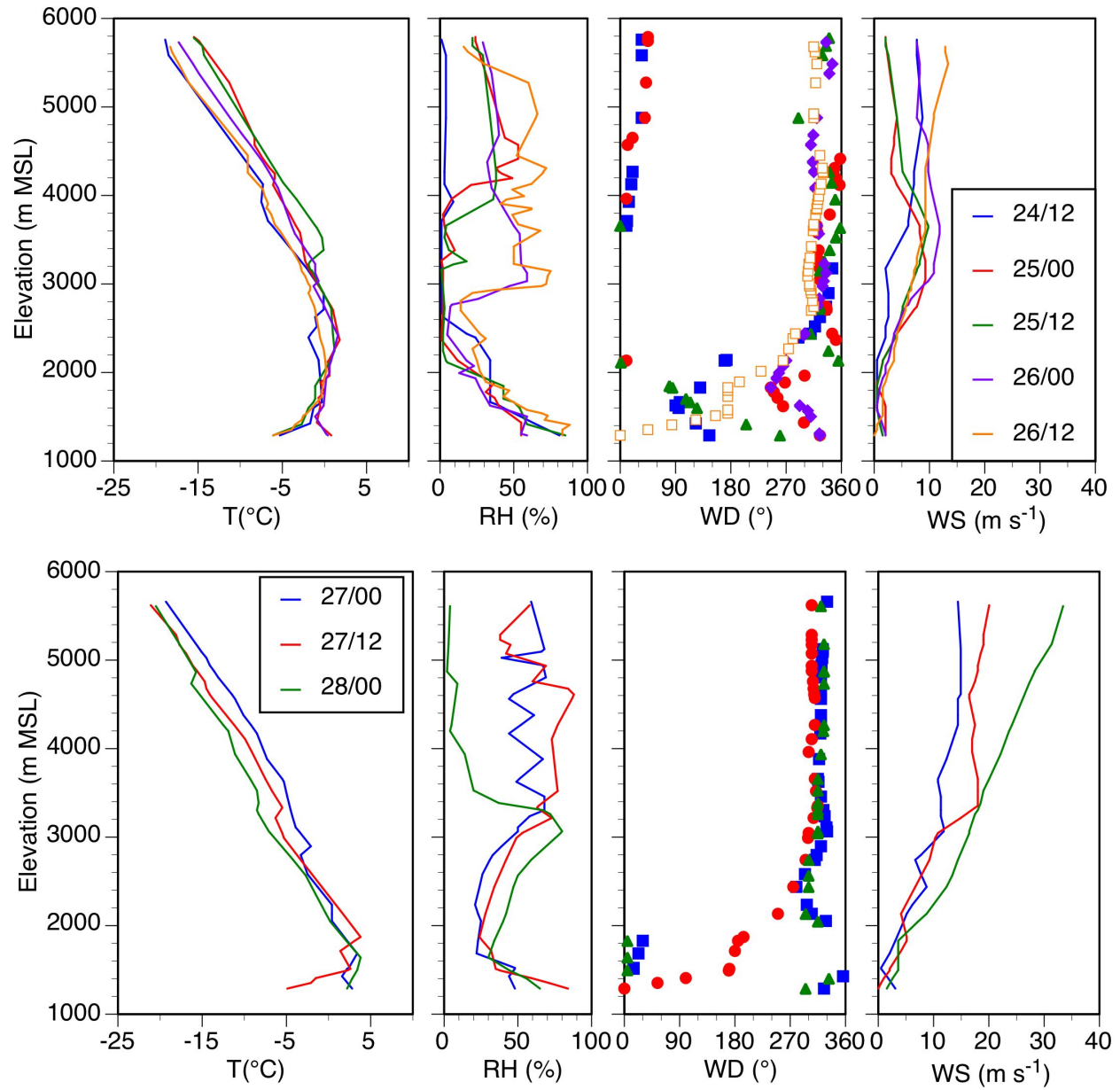Figure B2. Same as Figure B1, but for 0500 MST 19 January to 1700 MST 23 January 2014.

Figure B3. Same as Figure B1, but for 0500 MST 24 January to 1700 MST 27 January 2014
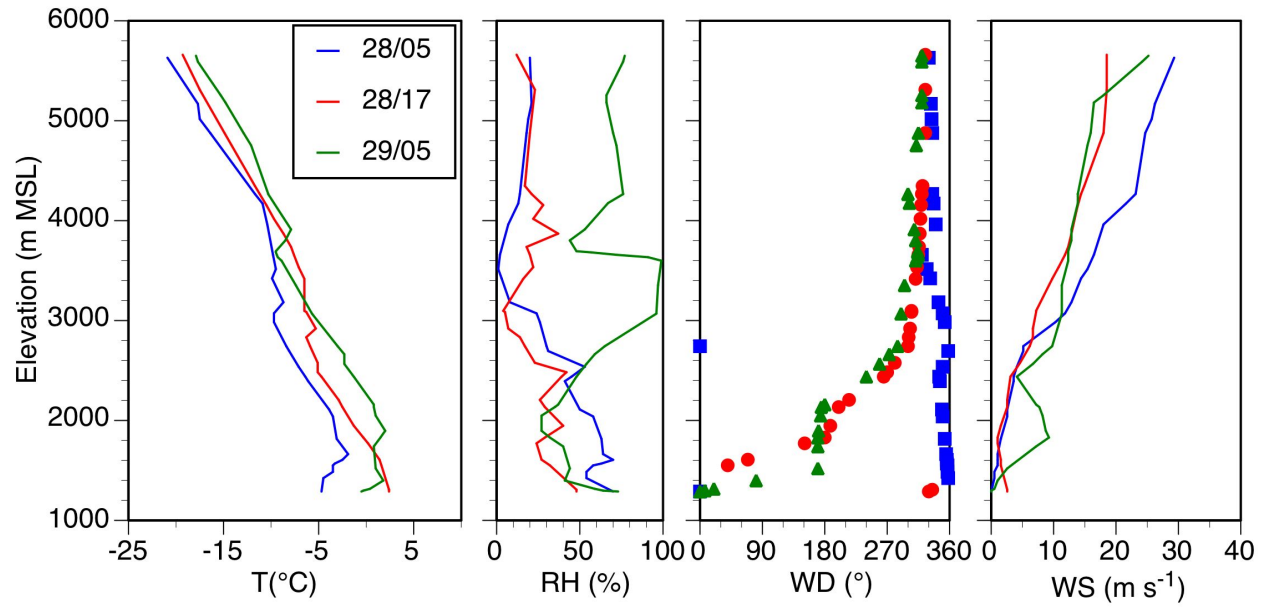
Figure B4. Same as Figure B1, but for 0500 MST 28 January to 0500 MST 29 January 2014.